3

Solid State Research

1969

Prepared under Electronic Systems Division Contract AF 19(628)-5167 by

Lincoln Laboratory

MASSACHUSETTS INSTITUTE OF TECHNOLOGY

Lexington, Massachusetts

3

Solid State Research

1969

Issued 23 October 1969

Prepared under Electronic Systems Division Contract AF 19(628)-5167 by

Lincoln Laboratory

MASSACHUSETTS INSTITUTE OF TECHNOLOGY

Lexington, Massachusetts

The work reported in this document was performed at Lincoln Laboratory, a center for research operated by Massachusetts Institute of Technology, with the support of the Department of the Air Force under Contract AF 19(628)-5167.

ABSTRACT

This report covers in detail the solid state research work at Lincoln Laboratory for the period 1 May through 31 July 1969. The topics covered are Solid State Device Research, Materials Research, and Physics of Solids.

Accepted for the Air Force
Franklin C. Hudson
Chief, Lincoln Laboratory Office

INTRODUCTION

1. SOLID STATE DEVICE RESEARCH

The temperature dependence of the energy of laser emission from $Pb_{1-x}Sn_xSe$ diodes in the composition range $0 \leqslant x \leqslant 0.3$ has been studied at temperatures up to 100°K. For $0 \leqslant x < 0.15$, the temperature dependence is positive and equal to $+5.0 \times 10^{-4}$ eV/°K above 30°K, whereas for $0.15 < x \leqslant 0.3$ the temperature coefficient is negative and about the same magnitude. This is consistent with the band model proposed in which the conduction and valence bands invert and exchange roles at about $x = 0.15$ at low temperatures.

In addition, the magnetic field dependence of the energy of laser emission from $Pb_{1-x}Sn_xSe$ diodes in this composition range has been studied at 4.2°K in magnetic fields up to 145 kG. For $0 \leqslant x < 0.15$ the magnetic field dependence is positive for all emission lines observed and is equal to about $+1.0 \times 10^{-7}$ eV/G for the lowest energy line. For $0.15 < x \leqslant 0.3$, this coefficient has about the same absolute value but is negative. This is again consistent with the proposed band inversion model. The magnetic field data have been used to obtain information not only on the extremal conduction and valence bands but on the other bands in the vicinity of the energy gap as well.

Total ionized impurity densities from 7×10^{13} to 3×10^{17} cm^{-3} have been determined for epitaxial samples of n-type GaAs by analyzing mobility and carrier concentration data as a function of temperature using the Brooks-Herring formula for ionized impurity scattering. The procedure employed minimizes the effects of other scattering mechanisms and gives results which are in good agreement with impurity densities obtained from analyses of the temperature variation of the Hall constant. These results have been used to determine empirical curves relating the impurity density to the 77°K Hall mobility and carrier concentration measured at 5 kG.

The effect of donor concentration on the extrinsic photoconductivity spectra of shallow donors in GaAs has been studied for donor concentrations between 4.8×10^{13} and 2×10^{15} cm^{-3}. The photoconductivity peak corresponding to the impurity ground state to first excited state transition remains essentially constant at 4.41 meV, while the measured thermal ionization energy decreases from 5.52 to 3.29 meV over this same concentration range. The change in thermal ionization energy is thus attributed to the merging of the higher excited impurity states with the conduction band edge rather than to a shift in the ground state energy.

Spectral measurements have been made on electroluminescent metal-insulator-semiconductor (MIS) diodes fabricated from p-type ZnTe. The insulating region was created by proton bombardment, and gold was used for the metal contact. Both green and red electroluminescence was observed in devices made from different crystals. The green electroluminescence is associated with the bandgap and has a quantum efficiency of 2×10^{-4} at 300°K and 10^{-3} at 77°K. The red electroluminescence is associated with an isoelectronic trap due to oxygen impurities and has a quantum efficiency of 3×10^{-3} at 300°K and 4×10^{-3} at 77°K.

II. MATERIALS RESEARCH

Single crystals of EuO, EuS, EuSe, and EuTe up to 2 cm on a side have been grown by slow cooling of Eu-rich solutions (or nominally stoichiometric melts, for EuO) in sealed tungsten crucibles. Thermal analysis has been used to determine the congruent melting point of EuO (2015°C).

Single crystals of NbO have been grown by pulling from the melt in a tri-arc furnace. The limits of the homogeneity range of NbO_x are approximately x = 0.98 and x = 1.02, and the congruently melting composition is x = 1.006.

The phase diagram of the CdTe-CdSe pseudobinary system has been determined by thermal analysis and x-ray diffraction measurements. Below the solidus curve, the diagram consists of Te- and Se-rich regions of alloys with zincblende and wurtzite structure, respectively, separated by a narrow two-phase region whose boundaries are strongly temperature dependent.

The Hall coefficient and resistivity of undoped CdSe single crystals have been measured at temperatures up to 950°C and at controlled cadmium vapor pressures between 100 and 700 torrs. Over the pressure range investigated, the results show that above 600°C the electrical properties are determined by the concentration of a doubly ionized native donor defect.

A large number of germanates and stannates with the $PbSb_2O_6$ structure have been prepared by sintering stoichiometric mixtures of oxides and carbonates. The optical properties of $MnGeTeO_6$ indicate that this compound contains, in addition to Mn^{2+}, a small amount of Mn^{4+} substituted for Ge^{4+}.

An x-ray diffraction study of $MnSb_2O_6$ has shown that this compound has a structure closely related to that of Na_2SiF_6, rather than the niobite structure reported previously. Data for a number of other oxides indicate that these also have structures related to the Na_2SiF_6 structure.

The relationship between structure and physical properties of the $M_xV_2O_5$-β phases (M = Cu, Li, Hg, Na, Ag) has been re-examined. The analysis, together with small polaron theory, gives an expression (containing no adjustable parameters) which is in excellent agreement with experimental data for the Seebeck coefficient as a function of x.

The first three atomic form factors of Ni have been determined by means of absolute x-ray intensity measurements on pressed powders. The results agree within experimental error with a set of published values obtained in transmission experiments on thin single crystals, rather than with a set obtained in earlier measurements on powders.

X-ray diffraction measurements at room temperature with diamond anvil cameras have shown that Cd_3As_2 and Zn_3As_2 transform at high pressures to similar trigonal phases. The high pressure phase of Cd_3As_2 could be retained at atmospheric pressure by cooling to low temperature before releasing the pressure, but this was not the case for Zn_3As_2.

Magnetic and optical measurements have been made on the atmospheric pressure and high pressure forms of $CsCoF_3$. The former exhibits antiferromagnetic ordering below 8°K, while the latter undergoes a ferrimagnetic transition at 50°K.

In order to improve the precision of chemical analyses which use EDTA titrations with color change end points, a method has been developed for performing these titrations automatically. In initial experiments on the determination of zinc, this automatic photometric method has achieved the same precision as a standard method employing automatic potentiometric titration.

III. PHYSICS OF SOLIDS

A comprehensive magneto-optical study of the conduction band of InSb has been carried out. Aside from the fundamental cyclotron resonance transitions, additional transitions involving impurities, spin-flip, cyclotron resonance harmonics and phonons were investigated.

Electron-phonon interactions were also investigated in CdTe with cyclotron resonance measurements at discrete laser and carcinotron wavelengths between 118 and 901 μ. The effective mass of the polarons was found to vary in the manner predicted from a variational calculation of the lowest Landau level energies.

Although the necks in the Fermi surface of copper have been clearly detected by positron annihilation studies, there is an apparent disagreement concerning the size of the necks as measured by various slit geometries. A single noninteracting particle calculation of the expected increase in the counting rate gives an estimate which is a factor of two smaller than the rectangular slit measurement, and somewhat larger than that of the point slit result.

The band structure study of magnetic semiconductors has now been extended to EuS and EuSe. Measurements as a function of temperature of the reflectivity of the peak associated with the fundamental absorption edge of these materials, using circularly polarized light and an orienting magnetic field, indicate a behavior similar to that of EuO and support the model proposed for the latter ferromagnetic semiconductor.

A new type of electron spin waves in nonmagnetic conductors has been predicted. These waves, which can exist even when explicit exchange interactions are unimportant, arise from spin-orbit coupling and the long range self-consistent field of the electrons.

Fine structure, which is a manifestation of an allowed linear dependence of the optical phonon frequency with wavevector, has been observed in the low temperature Raman spectrum of the 128-cm^{-1} E-mode in α-quartz. The optical activity which should be associated with this linear wavevector shift has been calculated.

A general calculation (which includes particle-particle Coulomb interactions, band structure of arbitrary nature, and virtual interband processes) has been made of the cross section for inelastic scattering of light from carriers in semiconductors placed in a magnetic field. The results encompass scattering from the longitudinal magnetoplasma collective modes, single particle excitations between Landau levels and spin states, spin density fluctuations, and spin waves.

CONTENTS

ORGANIZATION

SOLID STATE DIVISION

P. E. Tannenwald, *Acting Head*
M. J. Hudson, *Assistant*
E. P. Warekois
C. R. Grant

SOLID STATE THEORY

H. J. Zeiger, *Leader*
M. M. Litvak, *Assistant Leader*

Brine, N. S.
Chinn, S. R.*
Dresselhaus, G. F.
Hamilton, D. C.
Johnson, L. G.
Kaplan, T. A.
Kleiner, W. H.
Landon, S. N.
Larsen, D. M.
Palm, B. J.†
Sigel, J. L.
Wilson, A. R. M.

SOLID STATE PHYSICS

J. G. Mavroides, *Leader*
G. B. Wright, *Assistant Leader*

Allen, J. W.
Barch, W. E.
Blum, F. A.
Brandt, R. C.
Burke, J. W.
Crooker, P. P.
DeFeo, W. E.
Dresselhaus, M. S.†
Dwight, K., Jr.
Feinleib, J.
Feldman, B.
Groves, S. H.
Henrich, V. E.
Johnson, E. J.
Kernan, W. C.
Kolesar, D. F.
Krag, W. E.
Melngailis, J.
Menyuk, N.
Nill, K. W.
Parker, C. D.
Pine, A. S.
Scouler, W. J.
Waldman, J.*
Weber, R.

ELECTRONIC MATERIALS

J. B. Goodenough, *Leader*
A. J. Strauss, *Associate Leader*

Anderson, C. H., Jr.
Arnott, R. J.
Banus, M. D.
Batson, D. A.
Brebrick, R. F., Jr.
Button, M. J.
Capes, R. N.
Delaney, E. J.
England, R. E.
Fahey, R. E.
Finn, M. C.
Hilton, T. W.
Iseler, G. W.
Kafalas, J. A.
Kasper, H. M.
LaFleur, W. J.
Lavine, M. C.†
Longo, J. M.
Mastromattei, E. L.
O'Connor, J. R.
Owens, E. B.
Plonko, M. C.
Raccah, P. M.
Reed, T. B.
Roddy, J. T.
Searles, I. H.
Smith, F. T. J.
Stack, T. E.
Steininger, J. M.
Temkin, R. J.*
Wheatley, G. E.

APPLIED PHYSICS

J. O. Dimmock, *Leader*
T. C. Harman, *Assistant Leader*
I. Melngailis, *Assistant Leader*

Brueck, S.*
Calawa, A. R.
Carter, F. B.
Caswell, F. H.
Clough, T. F.
Donnelly, J. P.
Ferrante, G.
Foyt, A. G.
Krohn, L.
Lindley, W. T.
Mooradian, A.
Murphy, R. A.*
Oliver, M. R.*
Orphanos, W. G.
Paladino, A. E.
Spears, D. L.
Stillman, G. E.
Ward, J. G. R., III
Wolfe, C. M.
Woods, R.
Youtz, P.

---

* Research Assistant
† Part Time

REPORTS BY AUTHORS ENGAGED IN SOLID STATE RESEARCH

15 May through 15 August 1969

PUBLISHED REPORTS

Journal Articles*

JA No.			
3173A	Statistical Thermodynamics of Nonstoichiometry in Nonmetallic Binary Compounds	R. F. Brebrick	J. Solid State Chem. 1, 88 (1969)
3197	The ReO_3 Band Structure in the Tight-Binding Approximation	J. M. Honig J. O. Dimmock W. H. Kleiner	J. Chem. Phys. 50, 5232 (1969)
3308	Conditions for Microwave Radiation from Excited OH Λ-Doublet States	M. M. Litvak B. Zuckerman† D. F. Dickinson†	Astrophys. J. 156, 875 (1969)
3329	Isolation of Junction Devices in GaAs Using Proton Bombardment	A. G. Foyt W. T. Lindley C. M. Wolfe J. P. Donnelly	Solid-State Electron. 12, 209 (1969)
3340	Infrared Pumping of Interstellar OH	M. M. Litvak	Astrophys. J. 156, 471 (1969)
3346	A New Series of Rare Earth Garnets $Ln_3^{3+}M_2Li_3^{+}O_{12}$ (M = Te, W)	H. M. Kasper	Inorg. Chem. 8, 1000 (1969)
3394	Far Infrared and Submillimeter Impact Ionization Modulation	I. Melngailis P. E. Tannenwald	Proc. IEEE (Letters) 57, 806 (1969)
3437	The Effect of Pressure and B-Cation Size on the Crystal Structure of $CsBF_3$ Compounds (B = Mn, Fe, Co, Ni, Zn, Mg)	J. M. Longo J. A. Kafalas	J. Solid State Chem. 1, 103 (1969)
3447	Polymorphism in Selenospinels – A High Pressure Phase of $CdCr_2Se_4$	M. D. Banus M. C. Lavine	J. Solid State Chem. 1, 109 (1969)
3463	Temperature and Compositional Dependence of Laser Emission in $Pb_{1-x}Sn_xSe$	T. C. Harman A. R. Calawa I. Melngailis J. O. Dimmock	Appl. Phys. Letters 14, 333 (1969)

* Reprints available.

† Author not at Lincoln Laboratory.

JA No.			
3470	Spin Polarized Splittings in the Temperature Dependent Reflectance of EuO	J. Feinleib W. J. Scouler J. O. Dimmock J. Hanus T. B. Reed C. R. Pidgeon*	Phys. Rev. Letters 22, 1385 (1969)
3474	Polaron Zeeman Effect in AgBr	R. C. Brandt D. M. Larsen P. P. Crooker G. B. Wright	Phys. Rev. Letters 23, 240 (1969)
3475	Efficient Doping of GaAs by Se^+ Ion Implantation	A. G. Foyt J. P. Donnelly W. T. Lindley	Appl. Phys. Letters 14, 372 (1969)
3497	New Electron Spin Waves in Nonmagnetic Conductors	F. A. Blum	Phys. Rev. Letters 23, 73 (1969)
3507	Magnetic Field Dependence of Laser Emission in $Pb_{1-x}Sn_xSe$ Diodes	A. R. Calawa J. O. Dimmock T. C. Harman I. Melngailis	Phys. Rev. Letters 23, 7 (1969)
MS-2023	Electron Band Structure Studies Using Differential Optical Techniques and High Magnetic Fields	J. G. Mavroides	Chapter 8, Physics of Solids in Intense Magnetic Fields (Plenum Press, New York, 1969)
MS-2182	Fourier Expansion for the Deformation Potential in the Diamond Lattice	G. F. Dresselhaus M. S. Dresselhaus	Proc. 9th International Conference on Physics of Semiconductors, Vol. 1, (1968)
MS-2291	Fourier Expansions for Dispersion Relations in Semiconductors	G. F. Dresselhaus	
MS-2304	Laser Action and Photodetection in Lead-Tin Chalcogenides	I. Melngailis	Proc. International Colloquium on IV-VI Compounds [J. de Physique 29, C4-84 (1968)]
MS-2325	Thermal Brillouin Scattering Study of the Attenuation of Hypersound in Quartz	A. S. Pine	Light Scattering Spectra of Solids, G. B. Wright, ed., (Springer-Verlag, New York, 1969)
MS-2333	Raman Scattering from Lattice Vibrations of $GaAs_xP_{1-x}$	N. D. Strahm A. L. McWhorter	
MS-2334	Landau Level Raman Scattering	G. B. Wright P. L. Kelley S. H. Groves	
MS-2340	Tin Doping of Epitaxial Gallium Arsenide	C. M. Wolfe G. E. Stillman W. T. Lindley	Proc. 1968 Symposium on GaAs (Institute of Physics and The Physical Society, 1969)

* Author not at Lincoln Laboratory.

JA No.			
MS-2349	Deviations from Stoichiometry and Lattice Defects in lV-Vl Compounds and Their Alloys	A. J. Strauss R. F. Brebrick	J. de Physique (Supp.) 29, C4 (1968)
MS-2362A	The High Pressure Forms of $CsNiF_3$	J. M. Longo J. A. Kafalas	J. Appl. Phys. 40, 1601 (1969)
MS-2374	Distant-Neighbor B-B Interactions in Cobalt Chromite	K. Dwight N. Menyuk	J. Appl. Phys. 40, 1156 (1969)
MS-2377	Some Critical Properties of Quantum-Mechanical Heisenberg Ferro- and Antiferromagnets	H. E. Stanley	J. Appl. Phys. 40, 1546 (1969)
MS-2378A	Exact Solution for a Linear Chain of lsotropically-Interacting Classical Spins of Arbitrary Dimensionality	H. E. Stanley	Phys. Rev. 179, 570 (1969)
MS-2380	Pressure Effect Measurements Using a Vibrating-Coil Magnetometer	N. Menyuk J. A. Kafalas K. Dwight J. B. Goodenough	J. Appl. Phys. 40, 1324 (1969)
MS-2384	Band Structure of Magnetic Semiconductors	D. Adler J. Feinleib	J. Appl. Phys. 40, 1586 (1969)
MS-2385	Optical Studies and Band Structure of Cu-Ni Alloys	J. Feinleib W. J. Scouler J. Hanus	J. Appl. Phys. 40, 1400 (1969)

* * * * *

UNPUBLISHED REPORTS

Journal Articles

JA No.			
3429A	Avalanche Breakdown and Light Emission at Low-Angle Boundaries in n-ZnSe	J. P. Donnelly F. T. J. Smith	Accepted by Solid State Electron.
3444	Derivation of a Quasiparticle Transport Equation for an lmpure Fermi Liquid at Low Temperatures	J. L. Sigel	Accepted by Phys. Rev.
3483	X-ray Diffraction Studies on Cd_3As_2 and Zn_3As_2 at High Pressure	M. D. Banus M. C. Lavine	Accepted by High Temperatures-High Pressures
3485	Velocity and Attenuation of Hypersonic Waves in Liquid Nitrogen	A. S. Pine	Accepted by J. Chem. Phys.

JA No.			
3490	OH and H_2O Masers in Proto-stars	M. M. Litvak	Accepted by Science
3491	Perturbation of the Refractive Index of Absorbing Media by a Pulsed Laser Beam	P. R. Longaker M. M. Litvak	Accepted by J. Appl. Phys.
3498	Polarons Bound in a Coulomb Potential. I. Ground State	D. M. Larsen	Accepted by Phys. Rev.
3503A	Millimeter Wave Emission by Interstellar Dust	M. M. Litvak	Accepted by Nature
3541	Magnetic Ordering Effects on the Reflectivity of EuS and EuSe	C. R. Pidgeon* J. Feinleib W. J. Scouler J. Hanus J. O. Dimmock T. B. Reed	Accepted by Solid State Commun.
3548	A Conceptual Phase Diagram for Outer Electrons in Solids	J. B. Goodenough	Accepted as a chapter in Current Topics in Magnetism (Gordon and Breach, New York)
MS-2466	The Role of Oxygen Pressure in the Control and Measurement of Composition in 3d Metal Oxides	T. B. Reed	Accepted by J. Solid State Chem.
2506	Structural, Electrical and Magnetic Properties of Vacancy Stabilized Cubic 'TiO' and 'VO'	M. D. Banus T. B. Reed	Accepted by J. Solid State Chem.
2515	Evidence for a Continuous Sequence of Phases in the Bi-Te System	R. F. Brebrick	Accepted by J. Solid State Chem.

Meeting Speeches†

MS No.			
2349A,B	Deviations from Stoichiometry in IV-VI Compounds and Their Alloys	A. J. Strauss	Seminar, University of Pennsylvania, 21 May 1969; Summer Course, M.I.T., 1 July 1969
2466A	Stoichiometry of 3d Metal Oxides as a Function of Oxygen Pressure	T. B. Reed	Seminar, Purdue University, 20-21 May 1969
2496A	Pitfalls, Detours and Shortcuts on the Road to Single Crystal Growth	T. B. Reed	

* Author not at Lincoln Laboratory.

† Titles of Meeting Speeches are listed for information only. No copies are available for distribution.

Reports

MS No.			
2482A	Shubnikov-deHaas Measurements in $Pb_{1-x}Sn_xTe$	J. Melngailis	Seminar, Carnegie-Mellon University, Pittsburgh, Pennsylvania, 23 May 1969
2500	Spark Source Mass Spectroscopy	E.B. Owens	22nd Annual Summer Symposium on Analytical Chemistry, University of Georgia, 11-13 June 1969
2528A	Light Scattering Experiments at 1.06 Microns	A. Mooradian	Conference on Short Laser Pulses and Coherent Interactions, Chania, Crete, Greece, 13-26 July 1969
2608	Semiconductor Lasers	I. Melngailis	
2528C	Light Scattering Experiments at 1.06 Microns	A. Mooradian	Gordon Research Conference, Quantum Solids and Fluids, Providence Heights College, Issaquah, Washington, 21-25 July 1969
2617	One-Electron Theory of Interband Transitions	G. F. Dresselhaus	
2545	High Pressure Phases with Perovskite Related Structure in the System $Sr_{1+x}IrO_{3+x}(x = 0, 1/3, 1/2, 1)$	J. A. Kafalas J. M. Longo	8th International Congress of Crystallography, State University of New York, 14 August 1969
2549	Photoresponse Properties of InSb MOS Devices	W. E. Krag R. J. Phelan J. O. Dimmock	3rd International Conference on Photoconductivity, Stanford University, 12-15 August 1969
2551	Donor Magnetospectroscopy in High Purity Epitaxial GaAs	G. E. Stillman C. M. Wolfe J. O. Dimmock	
2575	Quantitative Analysis of Ternary and Quaternary Semiconducting Alloys	M. C. Finn	4th National Conference on Electron Microprobe Analysis (Electron Microprobe Society of America) Pasadena, California, 16-18 July 1969
2580	Tunable Long-Wavelength Infrared $Pb_{1-x}Sn_xSe$ Diode Lasers	A. R. Calawa I. Melngailis J. O. Dimmock T. C. Harman	Device Research Conference, University of Rochester, 23-26 June 1969
2581	MIS Electroluminescent Diodes in ZnTe	J. P. Donnelly A. G. Foyt W. T. Lindley	
2583	Extrinsic GaAs Photodetectors for the 100-400μ Region	G. E. Stillman C. M. Wolfe J. O. Dimmock	
2589	Interstellar Molecules	M. M. Litvak	Seminar, M. I. T., 16 May 1969

MS No.			
2590	Phase Diagrams and Crystal Growth of CdTe-ZnTe, CdTe-CdSe, and ZnTe-ZnSe Alloys	J. M. Steininger A. J. Strauss	Conference on Crystal Growth, Gaithersburg, Maryland, 11-13 August 1969
2594	Growth of EuO, EuS, EuSe, and EuTe Single Crystals	T. B. Reed R. E. Fahey	
2595	Film: Arc Crystal Growth and other Arc Materials Techniques	T. B. Reed M. D. Banus	
2598	Theory and Practice of Vapor Phase Crystal Growth	T. B. Reed	
2599	The Hartree-Fock Approximation	T. A. Kaplan	Seminar, M. I. T., 23 May 1969
2600	Maser Properties of Interstellar Molecules	M. M. Litvak	Joint Astrophysics and Center for Fluid Dynamics Seminar, Brown University, 27 May 1969
2609	Resistivity and Hall Effect (Technique and Interpretation)	A. J. Strauss	Summer Course, M. I. T., 1 July 1969
2625	Non-Equilibrium Processes Related to Interstellar Molecules	M. M. Litvak	Summer Course, M. I. T., 10 July 1969
2625A	Non-Equilibrium Processes Related to Interstellar Molecules	M. M. Litvak	Summer Institute, Brandeis University, 15 July 1969

I. SOLID STATE DEVICE RESEARCH

A. Temperature Dependence of Laser Emission in $Pb_{1-x}Sn_xSe$

In a previous report,[1] the variation of laser emission energy with temperature for three $Pb_{1-x}Sn_xSe$ diode lasers with x = 0.19, 0.218 and 0.276 was presented. The emission energy was observed to decrease as the temperature increased. Thus, a negative coefficient of energy gap was obtained for these compositions.

In this report we present the temperature dependences of laser emission energy of three $Pb_{1-x}Sn_xSe$ diode lasers with x = 0, 0.06, and 0.10. The results are displayed graphically in Fig. I-1. The temperature coefficient is very small at the lowest temperatures, whereas above about 30°K the coefficient is positive and approximately equal to $+5 \times 10^{-4}$ eV/°K for the three compositions. The change in sign of the temperature coefficient of the laser emission energy as x increases from 0.10 to 0.19 is predicted by the inverted energy bandgap model.[2]

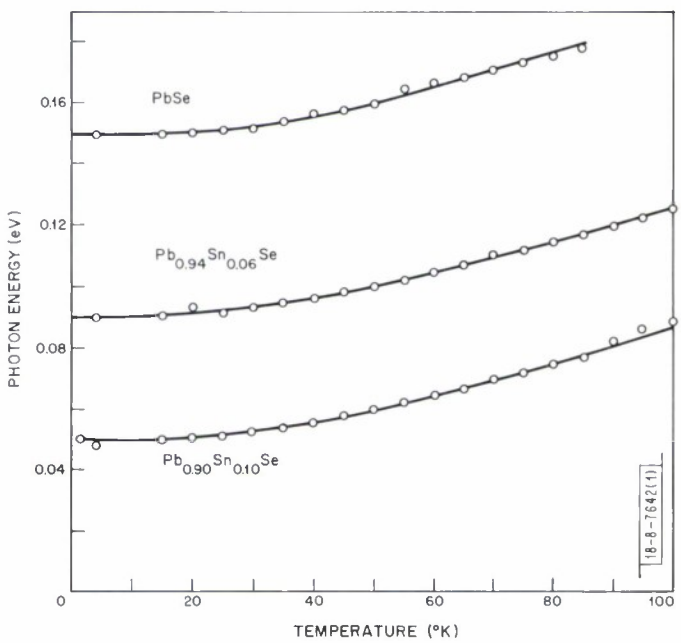

Fig. I-1. Temperature dependence of laser emission energy of $Pb_{1-x}Sn_xSe$ for x = 0, x = 0.06 and x = 0.10.

A recent theoretical calculation[3] of the temperature coefficient of the bandgap in PbTe has yielded a positive sign of approximately the observed magnitude. In addition, the calculation also predicts a negative sign for material in which the energy bands have become inverted. Since PbTe and PbSe are similar, the above results are expected to apply to the $Pb_{1-x}Sn_xTe$ alloy system as well.

T. C. Harman I. Melngailis
A. R. Calawa J. O. Dimmock

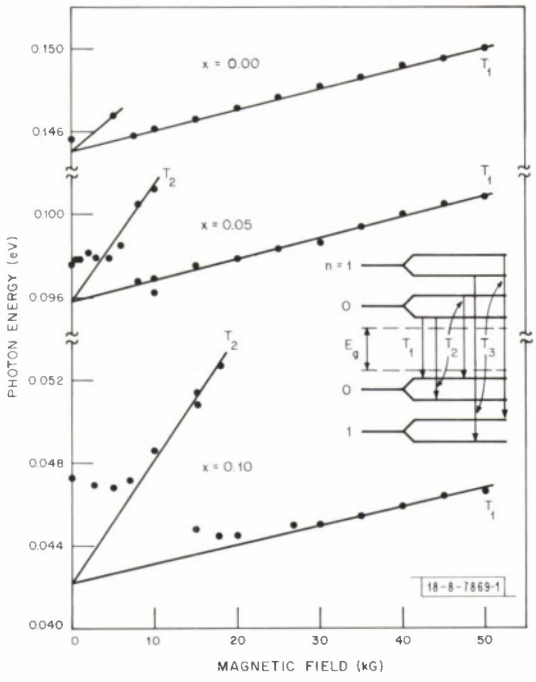

Fig. I-2. Magnetic field dependence af laser emissian in $Pb_{1-x}Sn_xSe$ diades with x = 0.00, 0.05 and 0.10 (data far PbSe, x = 0.00, was taken fram Ref. 2).

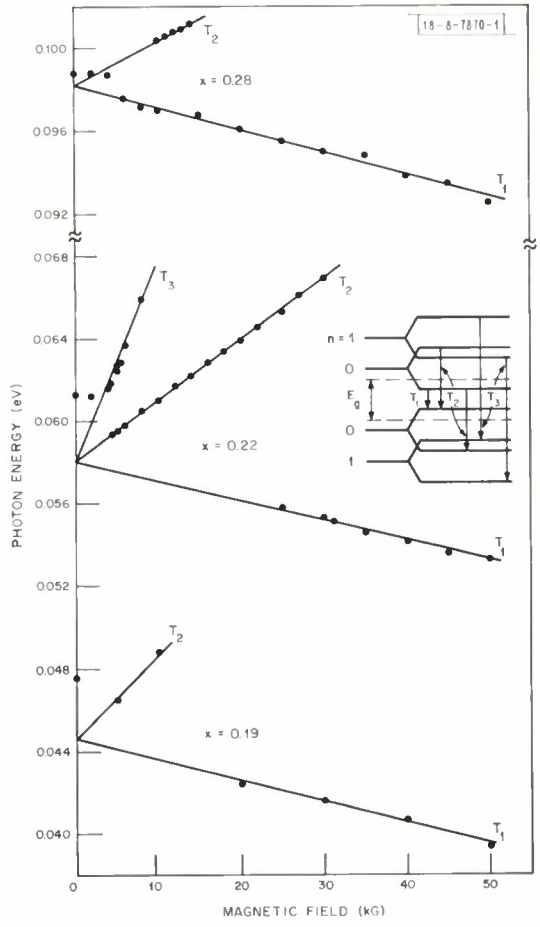

Fig. I-3. Magnetic field dependence af laser emissian in $Pb_{1-x}Sn_xSe$ diades with x = 0.19, 0.22 and 0.28.

B. Magnetic Field Dependence of Laser Emission in $Pb_{1-x}Sn_xSe$ Diodes

The magnetic field dependence of the energy of laser emission from $Pb_{1-x}Sn_xSe$ diodes with $x = 0.218$ and $x = 0.276$ has recently been reported.[4] Here the results of measurements made on an additional number of $Pb_{1-x}Sn_xSe$ diode lasers in the composition range $0 \leqslant x \leqslant 0.3$ at magnetic fields up to 145 kG are reported and the results discussed.

The photon energy of the laser emission as a function of magnetic field is shown in Fig. I-2 for diodes of $Pb_{1-x}Sn_xSe$ with $x = 0$, 0.05 and 0.10 and in Fig. I-3 for $x = 0.19$, 0.22 and 0.28. The Landau levels shown schematically in the insets identify the transitions observed. At low magnetic fields one generally observes the line T_2. As the field is increased the emission switches to T_1. If the diode current is increased the T_2 emission persists up to higher magnetic field values and in some cases a third line T_3 is observed.

For all of the alloys studied with $x < 0.15$ (including PbSe), the T_1 line is found to have a positive slope, in most cases about 10^{-7} eV/G. For alloys with $x > 0.15$ the slope of this line is negative but has about the same magnitude. The zero field energy gap as a function of alloy composition is shown in Fig. I-4. The mole fraction of SnSe(x) was measured using an electron microprobe, and the energy gap values were obtained from extrapolations of the magnetic field data to zero field as indicated in Figs. I-2 and I-3. The emission energy at zero magnetic field is generally 2 to 4 meV above this extrapolated value, probably due to band-filling.

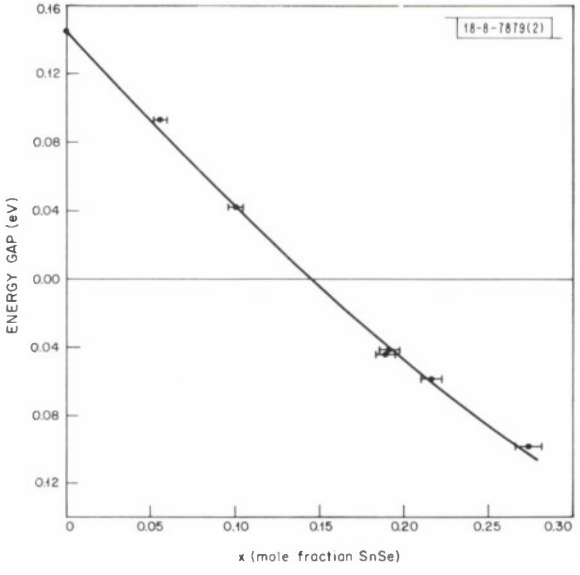

Fig. I-4. Energy gap vs composition in $Pb_{1-x}Sn_xSe$.

As we have indicated earlier,[4] the magnetic field dependence of the energy of the lower, T_1, laser emission line is determined entirely by the interaction of the extremal conduction and valence bands, L_6^- and L_6^+ respectively in PbSe, with higher energy conduction and lower energy valence bands at the L point in the Brillouin zone.[1] It is this effect which results in the change in sign of the magnetic field dependence when the conduction and valence bands become inverted for $x > 0.15$.

The fact that the absolute value of the slope of T_1 stays roughly constant with changing alloy composition from $x = 0$ to $x = 0.28$ indicates that the interactions of the L_6^+ and L_6^- bands with the more distant energy bands at the L point do not change much in this alloy range. This, combined with the observation that the relative energies of the L_6^+ and L_6^- bands change by 0.24 eV in this range, implies that the other energy bands are well separated from the conduction and valence bands. Energy band calculations[5, 6] indicate that this separation is of the order of 1 to 3 eV which is consistent with the above observations.

From the slope of T_1 we can obtain directly the quantity $2m_o/m_r^* - (g_c + g_v) \simeq 35$ where m_r^* is the reduced effective mass of the valence and conduction bands given by $(1/m_r^* = 1/m_c^* + 1/m_v^*)$ and m_v^*, m_c^*, g_v and g_c are the $\langle 100 \rangle$ band edge effective masses and g-factors of the

valence and conduction bands respectively. This quantity is a direct measurement of the interaction of the conduction and valence bands with the other bands at the L point.

As shown in Figs. I-2 and I-3 the next higher energy transitions following T_1 are the two transitions labeled T_2. No more than one T_2 line has been observed in any of the $Pb_{1-x}Sn_xSe$ diodes, and it has not been possible to determine if one transition or two equal energy transitions are involved. If the transitions have equal energies the two transitions labeled T_3 also have equal energies and a magnetic field dependence three times that of the T_2 line.

The highest energy emission line observed in $Pb_{0.78}Sn_{0.22}Se$ has approximately three times the slope of the T_2 line. We thus identify this line with the transition T_3. There are several allowed transitions with energies less than T_3. However, the probabilities for these transitions appear to be sufficiently smaller than those of T_3 and T_2 that their emission is not observed. Based on our identification of the T_1, T_2 and T_3 lines in $Pb_{0.78}Sn_{0.22}Se$ we can obtain $m_r^* = 0.018 \pm 0.001\, m_o$, $|g_c - g_v| = 9 \pm 9$, and $|g_c + g_v| = 78 \pm 8$ for this composition.

For the other diodes studied, present data were insufficient for a reasonably accurate determination of both mass and g-factor values. Nevertheless, for alloys with the same absolute value of the energy gap, those on the SnSe-rich side of the band inversion point appear to have a heavier effective mass than those on the PbSe-rich side. This can be understood qualitatively in terms of the positions of the other energy bands at the L point in PbSe.[5,6] The other energy bands which contribute significantly to the effective mass of the valence band all lie above the conduction band, and those which contribute significantly to the effective mass of the conduction band all lie below the valence band such that their effect is to decrease both the valence and conduction band masses, as compared with those predicted by the two-band model. However, when the conduction and valence bands invert, the effects of the other bands oppose those of the conduction and valence bands such that the masses are heavier than predicted by the two-band model.

For small energy gap alloys on the SnSe-rich side of the crossover the negative magnetic field dependence of the laser emission energy should enable the tuning of these lasers out to very long wavelengths. For $Pb_{0.81}Sn_{0.19}Se$ the T_1 line was observed up to 80 kG and 34 μ which is the longest wavelength semiconductor laser emission thus far obtained. However, the laser emission ceased at this point and was not observed at fields up to the maximum available field of 145 kG. For a second $Pb_{0.78}Sn_{0.22}Se$ diode, the T_1 line was observed to the maximum field, but at fields greater than 100 kG the magnetic field dependence deviated from a straight line with a diminishing slope.

It should be noted that according to Baraff the energy of this lowest transition is linear with magnetic field, except that there are higher order terms which prevent the two lowest magnetic levels from crossing. However, we can estimate that the minimum separation energy is of the order of 10^{-4} eV at 100 kG if indeed the other energy bands are 1 to 3 eV from the conduction and valence bands. This is much too small to account for the deviation in slope for the $Pb_{0.78}Sn_{0.22}Se$ diode emission. The situation is more complicated, of course, if the other energy bands are nearby.

A second possible cause for these effects arises from the fact that these diode lasers have bulk n and p-type carrier concentrations in the 10^{17} cm^{-3} to 10^{18} cm^{-3} range. The plasma energy for an alloy of composition x = 0.19 and a carrier concentration of 10^{18} cm^{-3} can be estimated to be approximately 0.034 eV or 37 μ which is in the energy range where these effects are occurring.

It should also be pointed out that we expect the cyclotron resonance energy to be in this same range at 100 kG for these low gap materials. One might expect an interaction with the plasma, magneto-plasma or cyclotron resonance modes which could affect the magnetic field dependence of the laser emission and possibly even the energy of emission at zero field. These possibilities are being studied further.

A. R. Calawa T. C. Harman
J. O. Dimmock I. Melngailis

C. Ionized Impurity Density in n-Type GaAs from 77°K Hall Measurements

Total ionized impurity densities ($N_D + N_A$) from 7×10^{13} to 3×10^{17} cm^{-3} have been determined for epitaxial samples of n-type GaAs by analyzing mobility and carrier concentration data as a function of temperature with the Brooks-Herring[7] formula for ionized impurity scattering. The procedure employed minimizes the effects of other scattering mechanisms and gives results which are in good agreement with impurity densities obtained from analyses of the temperature variation of the Hall constant. These results are then used to determine empirical curves relating the impurity density to the 77°K Hall mobility and carrier concentration measured at 5 kG.

The results of these mobility and Hall constant analyses are shown in Fig. I-5 together with the Hall mobility measured at 77°K (lower curve). The results of the analyses were terminated at 3×10^{17} cm^{-3} since there is no reason to expect the Brooks-Herring equation to be valid at higher concentrations. It can be seen that in the range ($N_D + N_A < 7 \times 10^{15}$ cm^{-3}) where both a

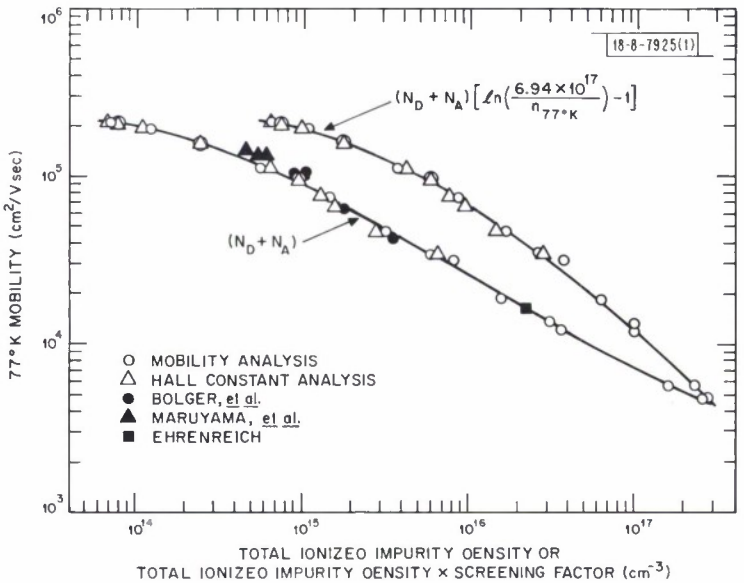

Fig. I-5. Empirical curves of total impurity density expected for o given 77° mobility.

Hall constant and a mobility analysis can be performed on the same sample, there is consistently good agreement between the two values. The results of other Hall constant analyses which were obtained under similar experimental conditions[8,9] together with the result of a variational calculation[10] are shown for comparison. (The low field Hall mobilities of Ref. 9 were normalized to 5 kG.)

To minimize variations due to screening (compensation ratios N_A/N_D varied from 0.20 to 0.65 for these samples), the same data were plotted as $(N_D + N_A)\,[\ln (6.94 \times 10^{17}/n) - 1]$ using the measured carrier concentration at 77 °K for n, where in the Brooks-Herring equation[7] we have assumed $b \gg 1$ and taken $n^* = n = N_D - N_A$. This is the upper curve in Fig. I-5. From this empirically derived curve it should be possible to obtain a good estimate of the ionized impurity concentration of a sample from a Hall constant and resistivity measurement at 77 °K.

Examples of the use of these curves are as follows: A sample with a 77 °K Hall mobility at 5 kG of 100,000 $cm^2/V\,sec$ from the lower curve has an $N_D + N_A$ of approximately $8 \times 10^{14}\,cm^{-3}$. At 100,000 $cm^2/V\,sec$ the ordinate for the upper curve is $5.1 \times 10^{15}\,cm^{-3}$. If the measured $n_{77\,°K} = 6 \times 10^{14}\,cm^{-3}$, then $(N_D + N_A) = 8.4 \times 10^{14}\,cm^{-3}$, whereas if $n_{77\,°K} = 1 \times 10^{14}\,cm^{-3}$, then $(N_D + N_A) = 6.5 \times 10^{14}\,cm^{-3}$.

The largest errors in the values of ionized impurity density determined from Fig. I-5 are expected as a result of experimental errors, variations in Hall factor with temperature and concentration, and the effects of other relevant scattering mechanisms. An examination of these effects indicates that the error in the estimate of ionized impurity density from Fig. I-5 should be within the scatter of the data which is at most about 20 percent.

For comparison, the procedure of estimating a lattice scattering limit at 77 °K (230,000 $cm^2/V\,sec$), simply combining this with the ionized impurity mobility, and determining the impurity content from the experimental mobility at 77 °K gives results which are in good agreement with Fig. I-5 for total impurity densities greater than about $5 \times 10^{16}\,cm^{-3}$ or less than about $1 \times 10^{14}\,cm^{-3}$. At intermediate concentrations, however, differences as high as 80 percent are obtained. Also, for comparison, the process of analyzing the mobility with the Brooks-Herring equation at a fixed lower temperature (20 °K) gives reasonable agreement with the results of Fig. I-5 over a narrow intermediate concentration range and differs by as much as 90 percent at low concentrations and as high as 200 percent at high concentrations.

C. M. Wolfe
G. E. Stillman
J. O. Dimmock

D. Effect of Donor Density on Extrinsic GaAs Photodetectors

We have previously shown that the dominant peak observed in the extrinsic photoconductivity spectra of high purity n-type GaAs is due to photoexcitation of electrons from the ground state to the first excited state of the shallow hydrogenic donors, followed by subsequent thermal ionization into the conduction band.[11] Measurements of the variation of the photoconductivity spectra with donor concentration over the range from $N_D = 4.80 \times 10^{13}$ to $2.06 \times 10^{15}\,cm^{-3}$ indicate that the photoionization energy remains essentially constant at 5.86 meV while the thermal ionization energy decreases from 5.52 to 3.29 meV over this same range.

Each sample was characterized electrically by analyzing Hall effect measurements as a function of temperature before the photoconductivity spectra were evaluated. The Hall effect measurements were made on symmetrically shaped samples using the van der Pauw technique.[12] Sn contacts were applied to the samples by alloying in a reducing atmosphere. The resulting contacts were ohmic at all temperatures at low electric fields and the same contacts were used for the photoconductivity measurements. The Hall constant was measured using a magnetic field of 5 kG and the carrier concentration was calculated assuming a Hall factor r = 1.

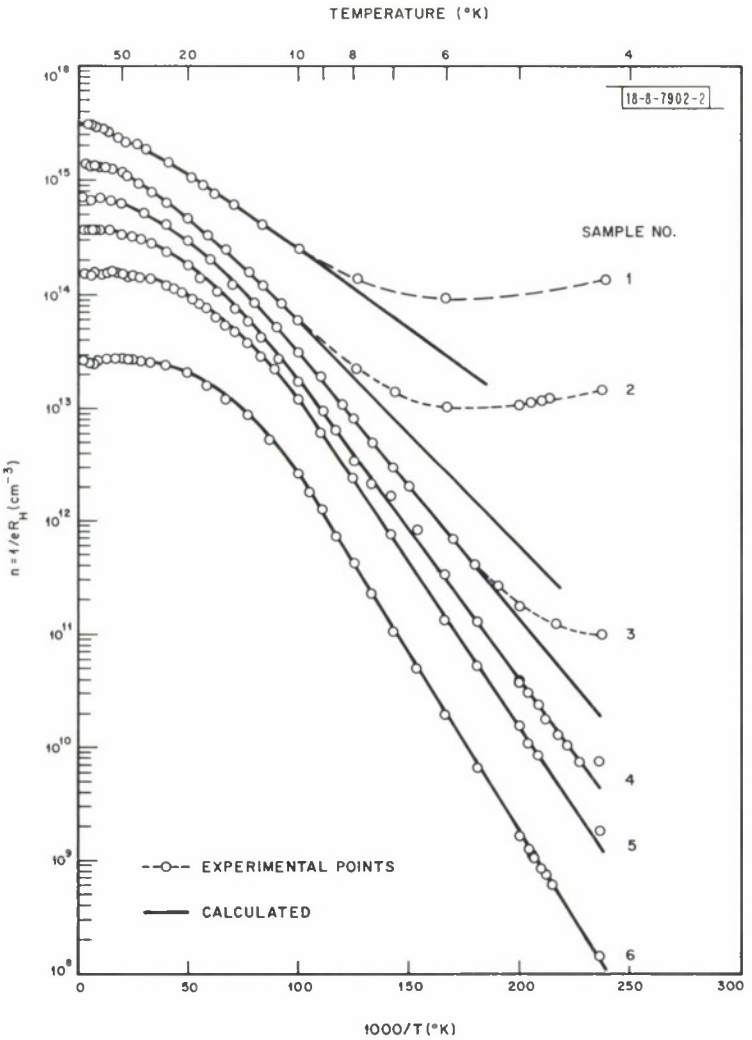

Fig. I-6. Electron concentration as a function of temperature for GaAs samples with donor concentrations from 4.72×10^{15} to $4.8 \times 10^{13} cm^{-3}$.

The resulting variation of carrier concentration with temperature was then analyzed using the usual single donor statistics, neglecting excited states. The results of the Hall effect measurements and analyses for six samples are shown in Fig. I-6. These samples were selected because they cover fairly uniformly the range of donor concentrations over which photoconductive response has been observed. The circles are from the experimental data while the solid curves are the least squares fits to the experimental data using the equation

$$\frac{n(N_A + n)}{(N_D - N_A - n)} = \frac{N_c}{g} e^{-E_{Dt}/kT} .$$

The good fits at intermediate temperatures (10° to 50°K) indicate that it is not necessary to include the excited states in the calculation. In any event, neglecting the excited states has no effect on the value of E_{Dt} thus obtained, since this is determined mainly by the linear parts of the curves below about 10°K.

TABLE I-1

ELECTRICAL PROPERTIES OF EPITAXIAL GaAs SAMPLES AS DETERMINED FROM THE ANALYSES OF HALL EFFECT MEASUREMENTS

Sample	N_D (cm^{-3})	N_A (cm^{-3})	$n_{300°}$ (cm^{-3})	$\mu_{300°}$ ($cm^2/V\,sec$)	$\mu_{77°}$ ($cm^2/V\,sec$)	$n_{4.2°}$ (cm^{-3})	$\mu_{4.2°}$ ($cm^2/V\,sec$)	E_{Dt} ($10^{-3}eV$)
1	4.72×10^{15}	1.61×10^{15}	3.14×10^{15}	6,220	33,800	1.4×10^{14}*	415*	1.89
2	2.06×10^{15}	6.78×10^{14}	1.42×10^{15}	6,240	46,300	1.3×10^{13}*	495*	3.29
3	1.06×10^{15}	3.27×10^{14}	7.1×10^{14}	7,290	72,000	1.0×10^{11}*	2,000*	3.88
4	5.02×10^{14}	1.36×10^{14}	3.68×10^{14}	7,740	107,000	7.6×10^{9}	52,000	4.51
5	2.04×10^{14}	4.07×10^{13}	1.62×10^{14}	8,160	153,000	2.0×10^{9}	70,000	5.09
6	4.80×10^{13}	2.13×10^{13}	2.67×10^{13}	8,620	210,000	1.2×10^{8}	85,000	5.52

* These samples exhibited considerable impurity-band conduction at 4.2°K.

For samples 1, 2 and 3, impurity band conduction is observed at low temperatures, as indicated by the deviation of the experimental points from the calculated curve. The properties of these GaAs samples are summarized in Table I-1. The donor and acceptor concentrations present in these samples are the result of residual system impurities and no additional dopant was added. The results given for sample 6 represent nearly an order of magnitude reduction in total electrically active impurity content over previously reported GaAs, and samples of this purity have been reproducibly prepared using the $AsCl_3$-Ga-H_2 vapor epitaxial system.[13] The peak mobility for this sample was 340,000 cm^2/V sec at 40°K.

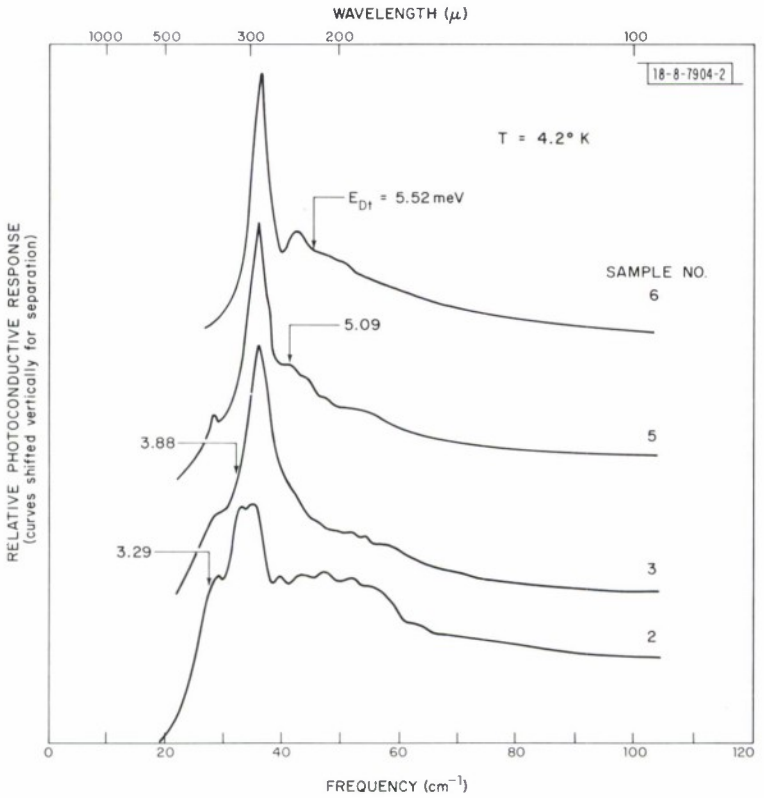

Fig. I-7. Donor concentration dependence of far-infrared photoconductivity spectra for GaAs at 4.2°K. E_{Dt} is the thermal ionization energy in meV for respective samples.

The photoconductivity spectra for four of the samples are shown in Fig. I-7. These spectra were normalized at the peak of the photoconductivity, and the curves were then shifted vertically for clarity. The absolute value of the responsivity decreased from sample 6 to sample 2, with the peak responsivity of sample 6 more than three orders of magnitude greater than that of sample 2.

The significant features of the spectrum for sample 6 are the large peak at 35.5 cm^{-1}, the smaller peak at 42.2 cm^{-1}, due to photoexcitation of electrons to the 2p and 3p excited states of the shallow donor respectively, and the broad continuum at higher frequencies. As the donor concentration is increased to $N_D \simeq 1 \times 10^{15} cm^{-3}$, the peak at 42.2 cm^{-1} merges with the continuum while the large peak at 35.5 cm^{-1} broadens appreciably but remains at the same frequency.

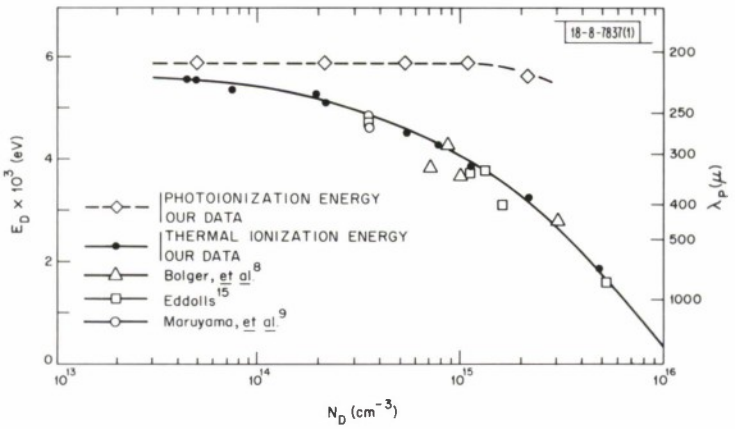

Fig. I-8. Concentration dependence of donor thermal ionization energy E_{Dt} and donor photoionization energy $E_I = 1.24/\lambda_p(\mu)$, for GaAs.

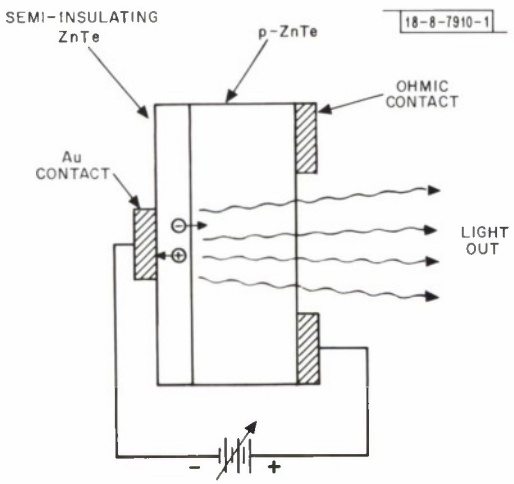

Fig. I-9. MIS electroluminescent ZnTe diode.

The small increase in N_D from 1.06×10^{15} to $2.06 \times 10^{15} cm^{-3}$ causes considerable broadening and a noticeable shift of the large peak to lower frequencies. For the latter sample the absolute value of the photoconductive response was drastically reduced. For sample 1, with $N_D = 4.72 \times 10^{15} cm^{-3}$, no photoconductive response was observed. The additional structure which appears for the samples with larger N_D has not been identified, but is possibly due to interactions between different impurity atoms.

Also shown in this figure are the thermal ionization energies in meV determined from the Hall effect analyses. Contrary to what has been previously reported,[14] it is obvious that the donor thermal ionization energy E_{DT} has no relationship whatever to the peak of the photoconductive spectra. The variation of the photoionization energy as calculated using the hydrogenic model and the energy of the (1s → 2p) transition is compared with the thermal ionization energy in Fig. I-8. For $N_D = 4.80 \times 10^{13} cm^{-3}$, the photoionization energy is 5.86 meV while the thermal ionization energy is 5.52 meV. The reason for this discrepancy is that the wave functions for the higher excited states overlap to form a band which merges with the conduction band.

To explain the difference between the observed thermal ionization energy and the calculated binding energy for this sample, only excited states higher than the 4th need to be merged with the conduction band. The thermal ionization energy decreases markedly at higher donor concentrations as the lower excited impurity states overlap and merge with the conduction band. However, the photoionization energy, as determined by the 1s → 2p photoconductivity peak, remains constant up to $N_D = 1 \times 10^{15} cm^{-3}$.

G. E. Stillman
C. M. Wolfe
J. O. Dimmock

E. MIS Electroluminescent Diodes in ZnTe

We have previously reported that proton bombardment can be used to create high resistivity layers in p-ZnTe[16] and that this technique can be used to fabricate MIS (metal-insulator-semiconductor) avalanching electroluminescent diodes.[17] In this report, we give a more detailed discussion of the fabrication and electroluminescent properties of these diodes.

The ZnTe samples used in most of our experiments were annealed solution-grown crystals with a room temperature carrier concentration of $2 \times 10^{16}/cm^3$ and a mobility of $80\ cm^2/V\ sec$. Following polishing and etching, each sample was bombarded at room temperature with a beam of mono-energetic protons. The energy of the protons ranged from 50 to 400 keV. After bombardment, gold contacts were evaporated on the samples. A dose of 5×10^{14} protons/cm^2 was sufficient to convert p-ZnTe with a carrier concentration as high as $2 \times 10^{18}/cm^3$ to semi-insulating material. From capacitance measurements it was determined that the depth of the semi-insulating layer varies linearly with incident proton energy and is approximately 1.2 μm for 100 keV protons. We have also examined samples on which an array of thin electroplated gold contacts was applied prior to bombardment, and have found little measurable difference in the results.

A typical electroluminescent diode is shown schematically in Fig. I-9. The diode thickness is approximately 100 μm and the top contact is a square 75 μm on a side. A hole has been opened in the back contact directly under the top contact to observe the electroluminescence. Before

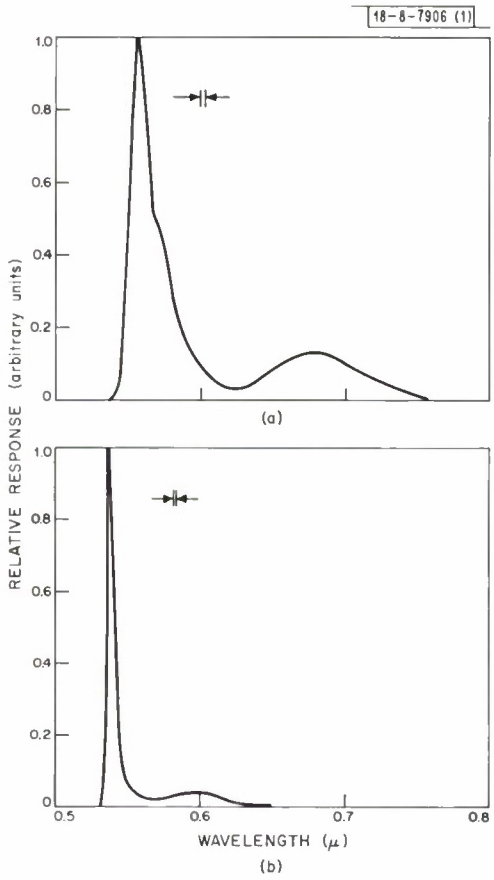

Fig. I-10. Spectrum of green ZnTe electroluminescent diode (a) 300°K, (b) 77°K.

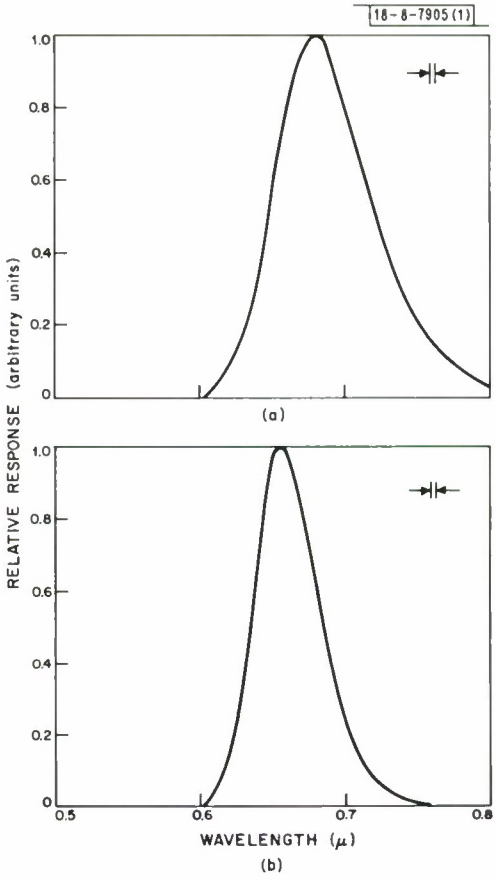

Fig. I-11. Spectrum of red ZnTe electroluminescent diode (a) 300°K, (b) 77°K.

bombardment, this structure exhibited ohmic behavior with a contact-contact resistance of about 200 ohms. After a bombardment of 5×10^{14} protons/cm^2, this resistance increased to a value over 10^9 ohms, from which the resistivity of the bombarded layer was estimated to be greater than 10^9 ohm-cm. Sharp avalanche breakdown was observed when the diode was biased in either direction. The forward bias (p-type substrate biased positively) breakdown voltage was usually a few volts less than the reverse breakdown voltage. Forward breakdown voltages ranged from approximately 6 volts for 50 keV proton bombardments to 80 volts for 400 keV proton bombardments.

Electroluminescence was observed through the opening in the back contact with current flowing in either bias direction. However, the quantum efficiency was found to be at least two or three orders of magnitude greater for current flowing in the forward bias direction. This difference is expected, since in forward bias, electrons created in the avalanche region are swept into the p-type region where efficient radiative recombination can take place. When the p-type substrate is biased negatively, however, electrons are swept toward the metal contact and radiative recombination is not expected, although some recombination does occur in the avalanche region.

Microscopic observation of these diodes showed that all the light is emitted directly below the top contact. It was also observed that the light is emitted from small distinct spots, indicating that the avalanche breakdown is occurring in filaments. In most good diodes, the light spots are distributed fairly uniformly over the diode. In some samples, however, only a relatively small number of filaments is observed. Although some filamentary behavior may be inherent in these avalanching devices, the variations noted from sample to sample seem to indicate that high field regions caused by crystal inhomogeneities are at present the major cause of this filamentary behavior.

Annealing studies have shown that the intrinsic layers created by proton bombardment anneal out sufficiently at 250°C to render these diodes inoperable. Although this temperature is low, it has only been a real problem in those devices where the current is carried by a few filaments. Here local hot spots can develop which result in diode burnout.

Two distinct types of MIS ZnTe electroluminescent diodes have been observed as characterized by their spectral output. For convenience, we refer to these as green and red diodes, respectively.

The spectrum of a green diode at room temperature and 77°K is shown in Fig. I-10. At 300°K, there is a green line at approximately 0.558 μ and a less intense broad red line at 0.685 μ. At 77°K, the green line narrows and shifts to 0.538 μ. Using a calibrated S-1 photomultiplier, we found that the light intensity emitted from the diode was proportional to the diode current for currents between 2 and 400 ma. The external quantum efficiency was approximately 2×10^{-4} at 300°K and 10^{-3} at 77°K. This green line is close to the bandgap energy and is characteristic of green photoluminescence observed in bulk p-type ZnTe.

Figure I-11 shows the spectrum of a red diode at room temperature and 77°K. At 300°K there is a broad red line at 0.685 μ, which narrows slightly at 77°K and shifts to 0.658 μ. The light intensity was again linear with diode current over the same current range. The quantum efficiency was approximately 3×10^{-3} at 300°K and 4×10^{-3} at 77°K. We have also noted that although the green diodes had an electroluminescent risetime of less than 100 ns, these red diodes exhibit an electroluminescence risetime of approximately 1.0 μs.

The wavelength, the relatively constant quantum efficiency between room temperature and 77°K, and the electroluminescent risetime of 1 μs suggest that the observed red electroluminescence is due to an oxygen isoelectronic trap.[18,19,20] Absorption and photoluminescent spectra corresponding to the oxygen trap have been observed in the samples showing this red line. Also, diodes fabricated from vapor grown substrates that were deliberately grown in an oxygen atmosphere have exhibited this characteristic red luminescence. Based on this evidence, we believe this red electroluminescence is due to the oxygen isoelectronic trap. At present we are trying to determine a correlation between quantum efficiency and oxygen concentration.

J. P. Donnelly
A. G. Foyt
W. T. Lindley

REFERENCES

1. Solid State Research Report, Lincoln Laboratory, M.I.T. (1969:1), p.12, DDC AD-687100; Appl. Phys. Letters 14, 333 (1969).
2. J.O. Dimmock, I. Melngailis and A.J. Strauss, Phys. Rev. Letters 16, 1193 (1966), DDC AD-642225.
3. C. Keffer, T.M. Hayes and A. Bienenstock, Phys. Rev. Letters 21, 1676 (1968).
4. Solid State Research Report, Lincoln Laboratory, M.I.T. (1969:1), p. 14, DDC AD-687100; Phys. Rev. Letters 23, 7 (1969).
5. P.J. Lin and L. Kleinman, Phys. Rev. 142, 478 (1966).
6. S. Rabii, Phys. Rev. 167, 801 (1968).
7. H. Brooks, Advan. Electronics Electron Physics 7, 158 (1955).
8. D.E. Bolger, J. Franks, J. Gordon and J. Whitaker, Proc. International Symp. GaAs, Reading, 1966, (Institute of Physics and The Physical Society, London, 1967), p. 16.
9. M. Maruyama, S. Kikuchi and O. Mizuno, J. Electrochem. Soc. 116, 413 (1969).
10. H. Ehrenreich, Phys. Rev. 120, 1951 (1960).
11. Solid State Research Report, Lincoln Laboratory, M.I.T. (1969:2), p. 1, DDC AD-690997. Solid State Communications 7, 921 (1969).
12. L.J. van der Pauw, Philips Res. Repts. 13, 1 (1958).
13. Solid State Research Report, Lincoln Laboratory, M.I.T. (1969:1), p.8, DDC AD-687100.
14. D.R. Bosomworth, R.S. Crandall and R.E. Enstrom, Phys. Letters 28A, 320 (1968).
15. D.V. Eddolls, Phys. Stat. Sol. 17, 67 (1966).
16. Solid State Research Report, Lincoln Laboratory, M.I.T. (1968:3), p. 10, DDC AD-678534.
17. Solid State Research Report, Lincoln Laboratory, M.I.T. (1969:2), p.4, DDC AD-690997.
18. R.E. Dietz, D.G. Thomas and J.J. Hopfield, Phys. Rev. Letters 8, 391 (1962).
19. J.D. Cuthbert and D.G. Thomas, Phys. Rev. 154, 763 (1967).
20. J.L. Merz, Phys. Rev. 176, 961 (1968).

II. MATERIALS RESEARCH

A. GROWTH OF EuO, EuS, EuSe AND EuTe SINGLE CRYSTALS

The divalent europium chalcogenides, which have the rock salt cubic structure, are of considerable current interest as magnetic semiconductors which are transparent in the infrared. The growth of EuO crystals from metal-rich solution was first described by Guerci and Shafer.[1] We have grown crystals of all four of these compounds up to 2 cm on a side by slowly cooling either metal-rich solutions or stoichiometric melts in tungsten or molybdenum crucibles. The synthesis and growth of EuO are described in detail in this section, and variations in technique used for EuS, EuSe and EuTe are then noted.

There appears to be a significant vapor pressure of Eu over EuO at elevated temperatures, necessitating that work be done in a sealed system. The tungsten crucibles used are 3 inches long and either 0.5 inch in diameter × 0.020-inch wall (total charge about 25 g) or 1 inch in diameter × 0.060-inch wall (total charge about 85 g). They are supplied with "insertion" lids, which are welded in an argon atmosphere by means of a laboratory arc melter[2] at a current of about 100 amps. During welding the crucible is held in a water-cooled cylindrical anode, which restricts melting to a narrow zone and keeps the charge cool.

Synthesis and growth from solution are accomplished by sealing Eu_2O_3 (dried at 1000 °C in vacuum and pressed into pellets) together with a 50 percent excess of Eu metal into a crucible. One or two crucibles are mounted in a cylindrical molybdenum block (with a small sighting hole drilled through one wall) inside a resistance furnace[3] with tantalum or tungsten heating elements, as shown in Fig. II-1. With one atmosphere of argon flowing through the furnace at 30 cm^3/min. the temperature is slowly raised to about 2300 °C. The furnace is then cooled at about 10 °C/hr to 1200 °C and at 20 °C/hr to room temperature.

After cooling, the crucible is very brittle and can be removed by gently cracking and peeling it from the ingot, which adheres to it because of the excess metal. The lower two-thirds of the ingot is generally single crystal with marked cubic cleavage perpendicular to the ⟨100⟩ axis. Although it is difficult to remove the crystal from the crucible without some cracking, cubes up to 2 cm on an edge and weighing over 20 g have been recovered. Above the crystal there is a two-phase region of leathery texture, and above this a layer of excess Eu metal.

The EuO crystals are moderately stable in air but tarnish noticeably in a few weeks. Mass spectrographic analysis of a typical crystal shows Ca = 1600, C = 210, Gd = 40, Sr = 40, Yb = 20, Dy = 20, Fe = 10, all others < 10 atomic ppm.

Doped or undoped crystals have been grown from the synthesized compound by adding 10 percent excess Eu metal and a dopant if required, and refreezing in the same manner. Mass spectrographic analysis of the first-to-freeze portion of a crystal grown from a solution doped with 8000 atomic ppm Gd showed: Gd = 190, C = 90, Ca = 60, Yb = 40, N = 10, all others < 10 atomic ppm. Thus in the presence of excess metal, the effective distribution coefficient for Gd in EuO was 0.025. It can also be seen that the excess metal passing through the EuO a second time lowers the concentration of many impurities by an order of magnitude or more. The concentrations of impurities in the first-to-freeze and last-to-freeze portions of another crystal, grown from a solution doped with 5000 atomic ppm Gd, are shown in Fig. II-2.

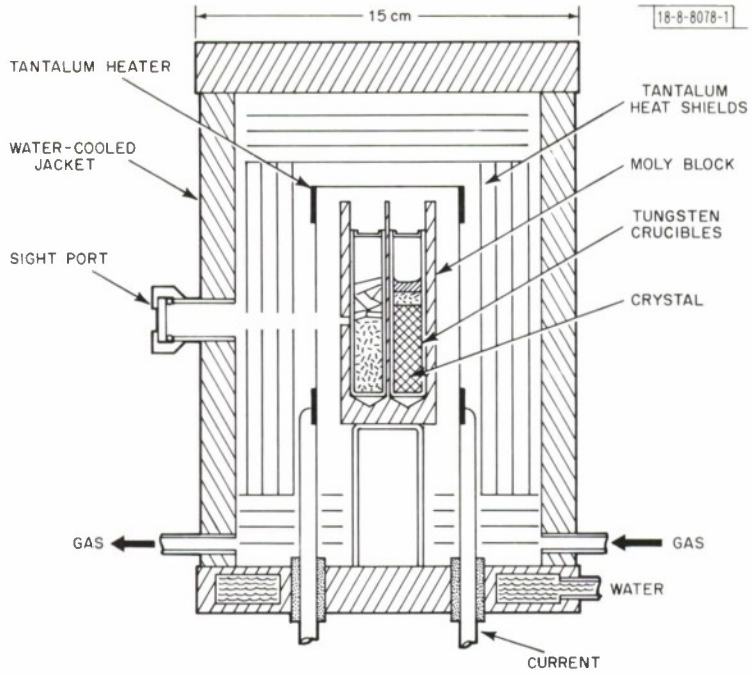

Fig. II-1. Apporotus for growth of Eu cholcogenide single crystols.

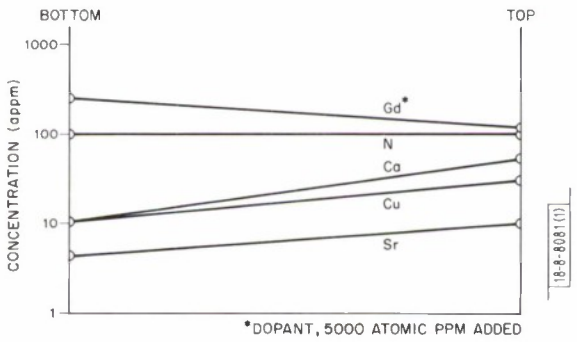

Fig. II-2. Impurity segregotion in EuO crystol grown from Eu-rich solution doped with 5000 otomic ppm Gd.

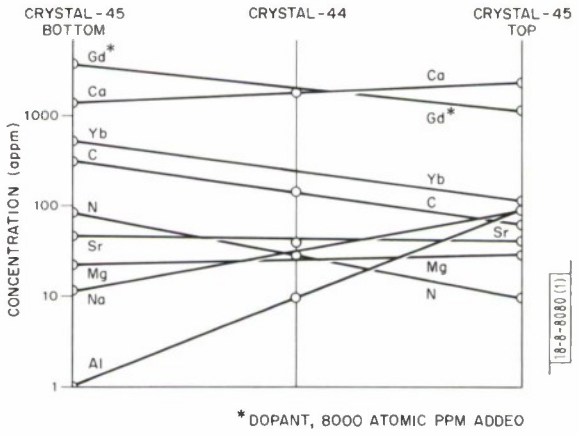

Fig. II-3. Impurity segregotion in EuO crystol (No. 45) grown from nominolly stoichiometric melt doped with 8000 otomic ppm Gd (impurity content of storting moteriol, crystol No. 44, is shown ot center of diogrom).

The sealed crucible method has also been employed to grow single crystals of EuO from nominally stoichiometric melts, by using the synthesized compound without adding excess Eu metal. The ingots obtained in this manner, which do not adhere to the crucible, do not contain a second phase of either Eu metal or another oxide. The formation of single phase material in this manner shows that EuO melts congruently. The melting point was determined by melting a single crystal in a sealed molybdenum crucible and measuring the temperature of the thermal arrest observed on cooling. The average value obtained in 7 cooling runs was 2015 ± 8°C.

The results of mass spectrographic analysis of a single crystal grown from a nominally stoichiometric melt doped with 8000 atomic ppm Gd are shown in Fig. II-3. It can be seen that the degree of purification is much less than that observed in growth from Eu-rich solution (Fig. II-2).

The homogeneity range of EuO is quite narrow and thus difficult to measure. Table II-1 summarizes the results of lattice parameter measurements on EuO crystals grown from solutions of various compositions. It also includes the values of x in EuO_x calculated from the weight gain observed on combustion of the samples in air or oxygen to Eu_2O_3. According to these results, there is a significant decrease in lattice parameter with increasing x.

TABLE II-1
LATTICE PARAMETER AND COMPOSITION OF EuO_x

Composition of Growth Solution	o_o (Å)	x
Large Eu excess	5.1450 ± 0.0005	0.970 ± 0.002
Small Eu excess	5.1431 ± 0.0005	1.000 ± 0.002
Stoichiometric (nominal)	5.1434 ± 0.0005	1.000 ± 0.002
Excess Eu_2O_3	5.1423 ± 0.0005	1.017 ± 0.002

In spite of the narrowness of the homogeneity range, changes in composition appear to have a significant effect on the optical and electrical properties of EuO. In general, undoped crystals grown from Eu-rich solution are highly transparent in the infrared from 2 to 10 μm, with absorption coefficients in this region of less than 1 cm^{-1}, while those grown from the melt have much larger absorption coefficients. The room temperature electrical resistivity of the last-to-freeze portions of doped and undoped crystals grown from solution is as low as 10^{-1} ohm-cm, while that of crystals grown from the melt is about 50 ohm-cm. The first-to-freeze portions of both solution and melt-grown crystals are insulating.

The other three Eu chalcogenides were synthesized by the method of Miller[4] and Holtzberg.[5] Chunks of Eu metal were placed at one end of a fused quartz tube and the stoichiometric amount of the chalcogen at the other end. After being evacuated and sealed, the tube was placed in a muffle furnace with the metal at about 600°C and the chalcogen in a cooler region near one end of the furnace, in order to prevent too rapid reaction. Over a period of several days the tube was moved to the center of the furnace, and after the reaction was almost complete the temperature was raised to 900°C. Crystals of all three compounds were grown from solution by adding

20 percent excess Eu metal to the synthesized material, heating to 2300°C, and cooling in sealed tungsten crucibles.

Attempts have been made to determine the melting points of EuS and EuSe by means of thermal analysis. Although thermal arrests at about 2070°C were observed on cooling, in subsequent experiments unmelted material was observed in crucibles which had been heated to much higher temperatures. From the latter results, it is concluded that the melting points of EuS and EuSe are higher than 2320°C. Similar experiments indicate that the melting point of EuTe is higher than 2250°C.

Crystals of the three compounds grown from Eu-rich solutions are almost opaque in the infrared, and their electrical resistivity at room temperature is of the order of 10^3 ohm-cm. These properties suggest the crystals contain excess Eu metal. Therefore EuS and EuSe crystals have been subjected to two annealing procedures designed to remove excess metal. After being annealed in a dynamic vacuum at 1600°C for 48 hours, the crystals became insulating and quite transparent in the infrared and red. Annealing at 1000°C for 64 hours in 1 atmosphere of S_2 or Se_2 vapor increased the resistivity to more than 10^6 ohm-cm but did not significantly increase the transmission.

T. B. Reed
R. E. Fahey

B. GROWTH AND PROPERTIES OF NbO SINGLE CRYSTALS

The compound NbO, like the closely related compounds TiO and VO, belongs to the class of transition metal oxides which exhibit metallic behavior. We summarize here the results of a detailed study[6] of NbO and compare them with results recently reported[7] for TiO and VO.

The structure of NbO can be viewed as rock salt cubic, with one Nb atom and one O atom missing at the corner and center of the unit cell. From this viewpoint, the NbO lattice has 25 percent ordered vacancies, whereas stoichiometric TiO and VO have a rock salt structure with about 15 percent random vacancies. Alternatively, NbO can be considered to have a simple cubic structure without vacancies, with Nb atoms at 1/2, 1/2, 0 and O atoms at 1/2, 0, 0, in fourfold coordination.

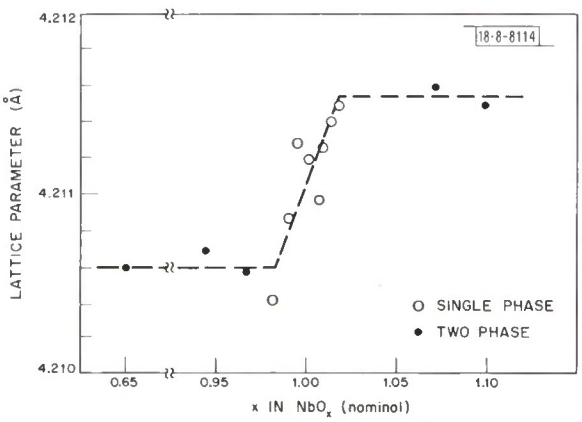

Fig. II-4. Lottice parometer as a function of nominal composition for NbO_x.

To determine the homogeneity range of NbO_x, samples with nominal compositions between x = 0.65 and x = 1.10 were synthesized from Nb and Nb_2O_5 in a tri-arc furnace.[8] The variation of lattice parameter with nominal composition, as plotted in Fig. II-4, shows that the limits of the homogeneity range are approximately x = 0.98 and x = 1.02. In contrast, TiO_x and VO_x are stable for approximately $0.8 < x < 1.3$, a range more than an order of magnitude wider.

Single crystals of NbO with compositions spanning the homogeneity range were pulled from the melt in the tri-arc furnace. They cleave easily, perpendicular to the ⟨100⟩ axis.

The composition was determined from the weight gain observed on combustion to Nb_2O_5 at 800°C for 16 hours. Comparison of the crystal and melt compositions showed the congruently melting composition to be x = 1.006 ± 0.002. The impurities found by mass spectrographic analysis were: C = 300, N = 400, Ta = 200, Fe = 90, Mo = 40, V = 10, all others <10 atomic ppm.

TABLE II-2

PROPERTIES OF $NbO_{1.00}$, $TiO_{1.00}$, AND $VO_{1.00}$

Property*	$NbO_{1.00}$	$TiO_{1.00}$	$VO_{1.00}$
Structure	NaCl cubic with 25 percent ordered voconcies, or simple cubic with no vacancies	NoCl cubic with 15 percent rondom vaconcies	NoCl cubic with 15 percent random vocancies
Lottice porometer (Å)	4.211	4.184	4.071
Density (g/cm^3)	7.24	5.00	5.60
Colar	Silver	Gold	Silver
Melting paint (°C)	1945	Incongruent	Incongruent
Resistivity (ohm-cm)			
300°K	20×10^{-6}	310×10^{-6}	720×10^{-6}
4.2°K	0.7×10^{-6}	–	1900×10^{-6}
Thermaelectric power (μV/°K)	<±1	−6.0	<±1
Magnetic susceptibility at 4.2°K (emu/mole)	116×10^{-6}	80×10^{-6}	300×10^{-6}
Superconducting transition temperature (°K)	1.45	0.8	Not detected down to 0.3°K

* At 300°K unless otherwise noted.

A variety of physical measurements have been made on the NbO crystals by standard techniques. The results for x = 1.00 are given in Table II-2, together with comparative data[7] for stoichiometric TiO and VO. The resistivity of $NbO_{0.982}$ is plotted against temperature in Fig. II-5, together with values at 4.2, 77, and 300°K for x = 1.001 and 1.008. The small values and the positive temperature coefficient of resistivity are characteristic metallic properties, as is the superconductive transition at 1.45°K. Figure II-6 shows the magnetoresistance of $NbO_{1.001}$ at 4.2°K as a function of magnetic field for two different orientations of the field.

E. R. Pollard*
T. B. Reed

*KEV Electronics Corporation, Wilmington, Mass.

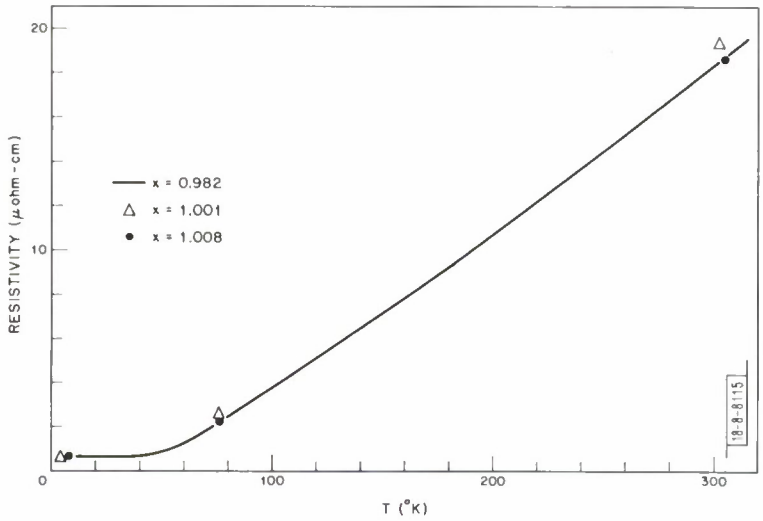

Fig. II-5. Resistivity as a function of temperature for single crystals of NbO_x analyzed by combustion to Nb_2O_5.

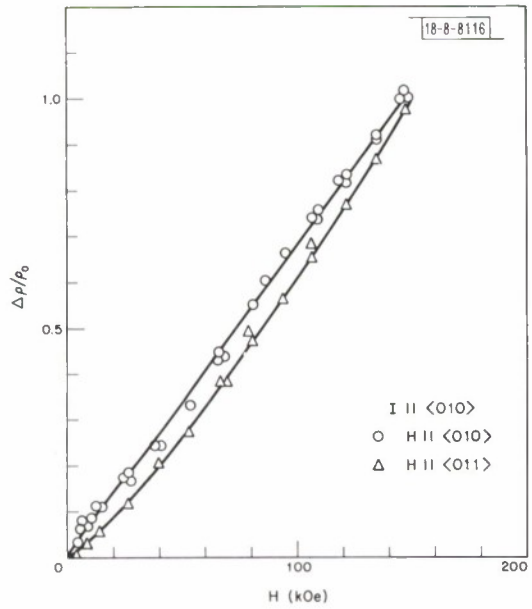

Fig. II-6. Magnetoresistance at 4.2°K as a function of magnetic field for a single crystal of $NbO_{1.001}$.

C. CdTe-CdSe PSEUDOBINARY SYSTEM

The stable high temperature phases of CdTe and CdSe have the cubic zincblende and hexagonal wurtzite crystal structures, respectively. X-ray diffraction studies[9-11] on samples prepared by solidification of alloy melts have shown that the compounds form pseudobinary solid solutions with zincblende structure at high Te content and wurtzite structure at high Se content. In the intermediate range of compositions between 30 and 70 mole percent CdSe, both structures have been obtained. No studies of the equilibria between the liquid and two solid phases have been reported.

We have determined the liquidus and solidus curves for the CdTe-CdSe system by differential thermal analysis, and have determined the phase boundaries between the solid phases by x-ray diffraction studies on samples which were annealed at high temperatures and then quenched.

Samples for thermal analysis were prepared by annealing mixed powders of CdTe and CdSe at 950 °C for 21 days or longer, until x-ray diffraction measurements indicated that they were homogeneous. The samples were then placed in fused silica ampoules and heated in a DTA apparatus described previously.[12] Solidus points were obtained from the thermal arrests which were observed either during initial heating of the annealed powders or during heating of the samples after they had been melted, frozen, and homogenized by annealing in the apparatus for 16 hours at about 20 °C below the solidus temperature. The two methods gave consistent results. Liquidus points were obtained from the thermal arrests observed when the samples were cooled after they had been melted and then homogenized for about 16 hours at about 50 °C above the liquidus temperature. Rates of 1 to 2 °C/min. were used for both heating and cooling.

The liquidus and solidus curves obtained by DTA are plotted in Fig. II-7. The dashed portion of the solidus is a theoretical curve calculated from the liquidus by using the liquidus-solidus equation for ideal, homogeneous, monotonic systems.[13] Both curves exhibit slow and smooth increases in temperature from the melting point of CdTe (1092 ± 0.2 °C) to that of CdSe (1252.5 ± 0.5 °C), except near pure CdTe, where there is an indication of a small decrease in temperature which suggests that the phase diagram is of the eutectic type. Both the temperature decrease and the separation between liquidus and solidus curves in this region are of the order of the experimental errors (±1 °or 2 °C). The eutectic composition appears to be below 20 mole percent CdSe and the eutectic temperature is 1091 ± 1 °C. Over the entire composition range of the system, the difference in mole fraction between the liquidus and solidus never exceeds 0.11.

The difference D between the partial excess free energies of mixing for equilibrium solidus and liquidus compositions in the CdTe-CdSe system has been calculated from the experimental data of Fig. II-7 by using the expression previously derived[13] for the general thermodynamic relationship between these two compositions in homogeneous, monotonic systems, together with the measured enthalpies of fusion of CdTe and CdSe.[14] For temperatures between the melting points of the pure compounds, the calculated values of D are small, of the order of 0.1 kcal/g-atom. This result indicates that the differences in deviations from ideality for the co-existent solid and liquid phases are also small. Therefore the solidus curve (given by the dashed line in Fig. II-7) calculated from the experimental liquidus data by using the ideal form[13] of the solidus-liquidus relationship is in excellent agreement with the experimental solidus data.

In order to determine the relationship between composition and structure for $CdTe_{1-x}Se_x$ solid solutions, x-ray diffraction measurements were made with a powder camera on samples

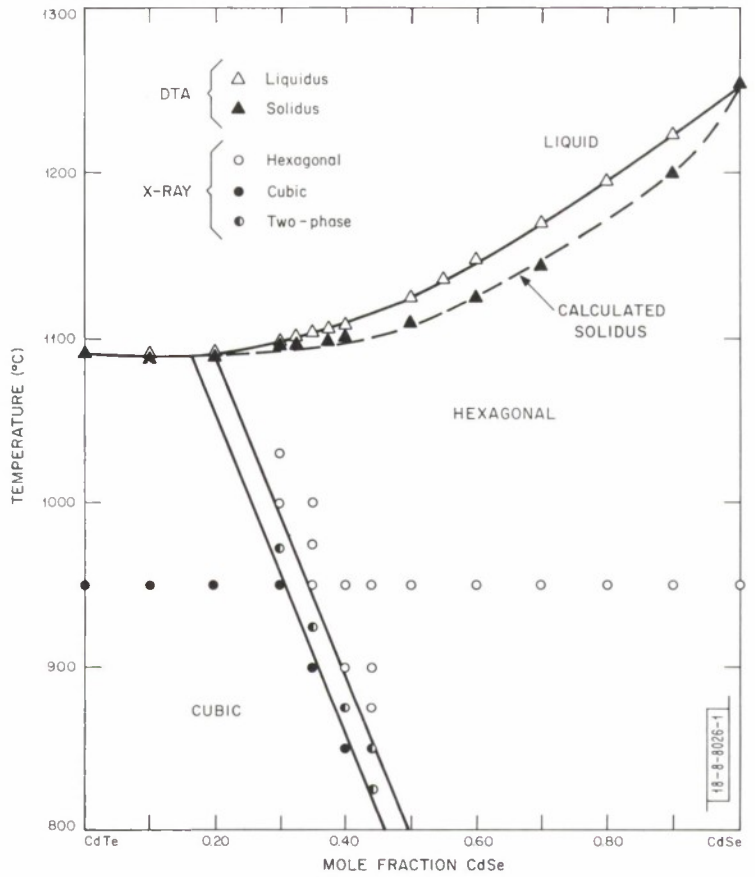

Fig. II-7. Phase diagram of CdTe-CdSe pseudobinary system.

which had been homogenized by long-term annealing in fused silica ampoules at 950°C and then quenched by dropping the ampoules into cold water. It was found that samples with $x \leqslant 0.3$ had the zincblende structure and those with $x \geqslant 0.4$ had the wurtzite structure, as shown in Fig. II-7. The volume per $CdTe_{1-x}Se_x$ "molecule" calculated from the measured lattice parameters varies almost linearly over the whole composition range from CdTe to CdSe, as shown in Fig. II-8.

The results of these annealing experiments appeared to be inconsistent with those obtained in crystal growth experiments, since melt-grown samples with x = 0.41 and 0.45 were cubic rather than hexagonal. The explanation for this discrepancy was suggested by the observation that an annealed sample with x = 0.44 which had been slow cooled due to furnace failure was also cubic. This indicated that over a certain composition range samples which were hexagonal at high temperatures could be transformed to cubic at lower temperatures.

To investigate the relationship between composition, temperature, and structure, homogeneous powdered samples with compositions of $0.25 < x < 0.50$ were annealed (usually for 24 hours) at temperatures between 800° and 1050°C and then quenched. The phases present were identified by means of x-ray diffractometer measurements. The results of these experiments, which are plotted in Fig. II-7, show that the single-phase hexagonal and cubic regions are separated by a narrow two-phase region whose boundaries depend on temperature. When extrapolated, these boundaries intersect the solidus curve near x = 0.17 and x = 0.20, in good agreement with

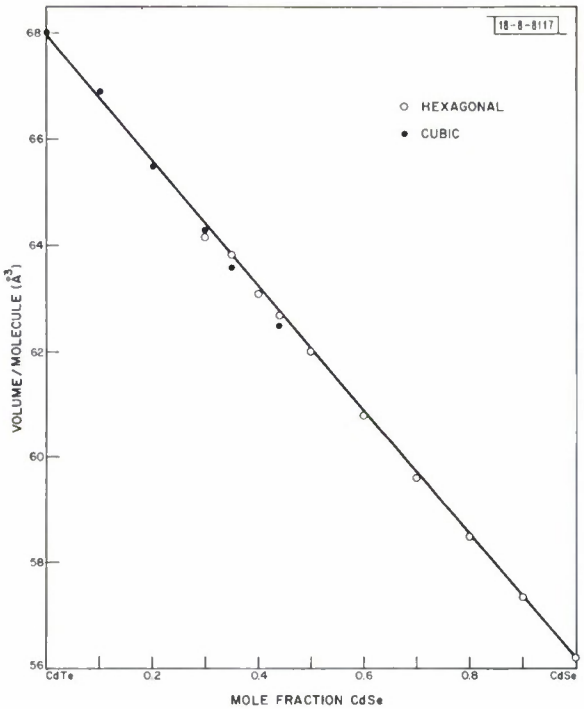

Fig. II-8. Volume per molecule os o function of composition for cubic and hexogonol solid solutions in CdTe-CdSe pseudobinory system.

the eutectic composition estimated from the DTA results. Thus the cubic structure is stable over the entire temperature range for $x \leqslant 0.17$, but only up to a certain maximum temperature for each higher CdSe composition.

J. M. Steininger
A. J. Strauss

D. ELECTRICAL PROPERTIES OF CdSe AT HIGH TEMPERATURES

Studies of the electrical properties of CdSe at room temperature and below have indicated that native defects play an important part in determining the carrier concentration.[15,16] Specimens quenched after equilibration at high temperature with cadmium vapor at partial pressures close to saturation are n-type with low resistivity. Specimens equilibrated close to selenium saturation and quenched arc semi-insulating. However, it has not been possible to characterize the native defect responsible for this behavior, since no simple relationship is observed between thc room temperature carrier concentration and the cadmium partial pressure during high temperature annealing. This situation has becn attributed to incomplete quenching of the high temperature equilibrium.

In order to avoid this difficulty we have made resistivity and Hall coefficient measurements at temperatures up to 950°C on undoped CdSe single crystals in an argon atmosphere containing controlled partial pressures of cadmium vapor.

The crystals were grown from Se-rich solution by the temperature gradient solution zoning technique.[17] Slices approximately 1 mm thick were annealed for two days at 850°C in molten cadmium in order to purify them by the solvent extraction process.[18] Mass spectrographic analyses after this treatment showed typical donor and acceptor concentrations of approximately 10^{17} cm^{-3}. The crystals had thc hexagonal wurtzite structure usually observed for CdSe. Since

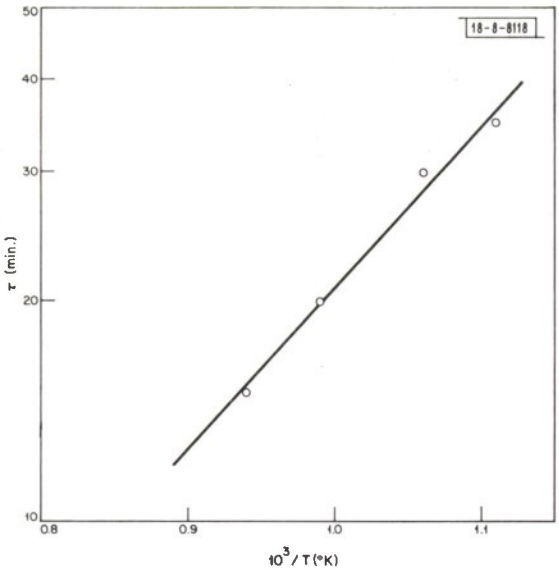

Fig. II-9. Temperature dependence af the time τ required for carrier cancentratian in CdSe ta reach equilibrium after a change in cadmium partial pressure.

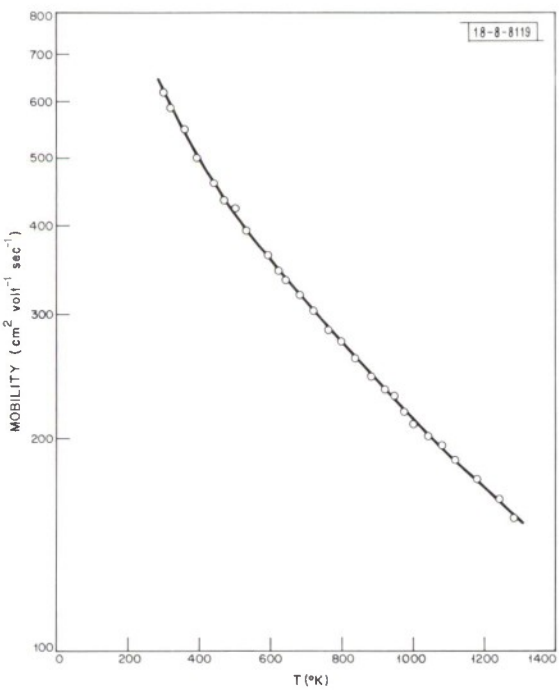

Fig. II-10. Hall mability af electrons in CdSe as a function of temperature.

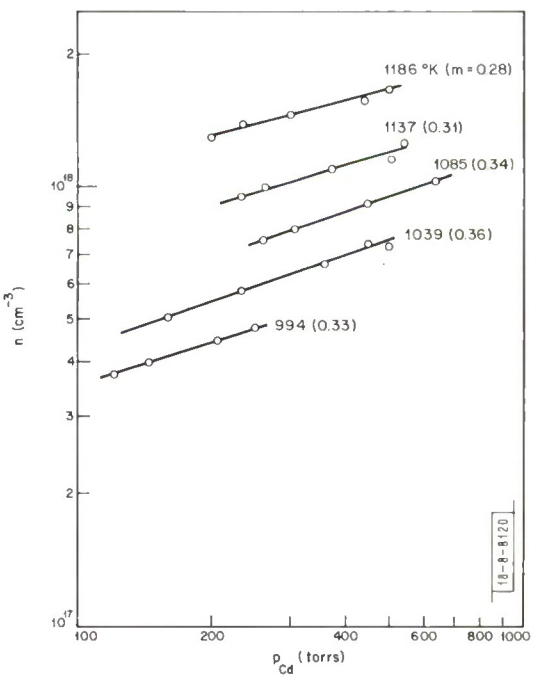

Fig. II-11. Equilibrium carrier concentratian (n) in CdSe at variaus temperatures as a functian af cadmium pressure (p_{Cd}). Slape af each line is given in parentheses.

the electrical properties of hexagonal CdSe are almost isotropic,[16] no specific crystallographic orientation was chosen.

The electrical measurements were made by the DC van der Pauw method in an apparatus described previously.[19] Contact was made to the sample by four graphite knife edges. The cadmium partial pressure was established by means of a pure cadmium reservoir, whose temperature was controlled independently of the sample temperature.

Each specimen was first heated to 750° to 800°C at a cadmium partial pressure approximately 20 percent of the saturated vapor pressure at the specimen temperature. After approximately 5 hours under these conditions, during which the specimen resistance increased approximately 10 percent, the resistance remained constant for periods of up to 48 hours at fixed cadmium partial pressure but showed an immediate response to changes in cadmium pressure. The initial stabilization may have resulted from the removal of cadmium precipitates from the previously cadmium-saturated specimens.

The time τ required to reach an equilibrium carrier concentration after a change in cadmium partial pressure decreased exponentially with increasing temperature, as shown in Fig. II-9. Since $D\tau \approx d/2$, where D is a diffusion coefficient (not necessarily that of the donor responsible for the measured carrier concentration) and d is the sample thickness, we obtain from the data of Fig. II-9 $D \approx 3.0 \times 10^{-4} \exp(-0.43\,eV/kT)$.

The Hall coefficient measurements showed the specimens to be n-type at all temperatures and cadmium partial pressures used. The measured Hall mobility for electrons is shown as a function of temperature in Fig. II-10. The mobility was reproducible from sample to sample and was independent of cadmium pressure or the thermal history of the specimen, as expected for lattice mobility. Over the temperature range investigated, the lattice mobility is probably limited by polar optical mode scattering.

Typical isotherms of equilibrium carrier concentration (n) vs cadmium partial pressure (p_{Cd}) are shown in Fig. II-11. These equilibrium values were reproducible and independent of the thermal history of the specimen. Throughout the temperature range of the experiments, 950° to 1250°K, $n \sim (p_{Cd})^m$. Such simple and reversible dependence of n on p_{Cd} can be explained satisfactorily only by the presence of a native donor defect which controls the carrier concentration. From the values of m given for each isotherm in Fig. II-11, an average value of $m = 0.31 \pm 0.03$ was obtained. This value indicates that the donor defect is doubly ionized, since the theoretical value of m is 1/3 for such a defect.[20] For a singly ionized defect, m would be 1/2.

Since the native donor concentration increases with cadmium partial pressure, the defect, if simple, may be either a cadmium interstitial or a selenium vacancy. Self-diffusion experiments[21] have indicated that a cadmium interstitial defect is present at appreciable concentrations in CdSe. However, the diffusion data show this defect to be singly ionized at high temperature, and therefore it is apparently not the defect which controls the electrical properties.

The lower curve in Fig. II-12 shows the carrier concentration as a function of reciprocal absolute temperature (1/T) at $p_{Cd} = 250$ torrs. The slope of this line is $\Delta H_f/3kT$, where ΔH_f is the apparent enthalpy of formation of the doubly ionized donor.[20] A value of 1.9 ± 0.2 eV for ΔH_f is obtained from the average slope for several values of p_{Cd}. This value is sufficiently close to the value of 1.7 eV which we have obtained by the same method for a doubly ionizable native donor in CdTe to suggest that the defects in the two compounds are similar.

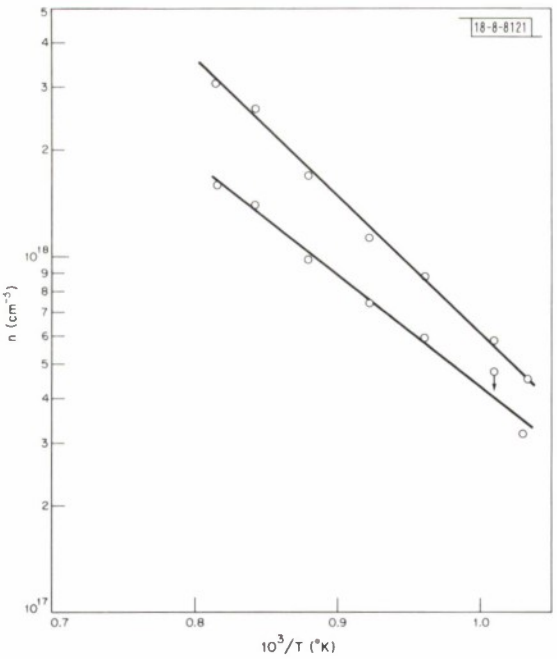

Fig. II-12. Corrier concentration in CdSe os o function of reciprocol obsolute temperature. Upper line: olong codmium-rich solidus; lower line: samples equilibroted ot p_{Cd} = 250 torrs.

The upper curve in Fig. II-12 shows the temperature dependence of the carrier concentrations obtained by extrapolating the isotherms of Fig. II-11 to the saturation vapor pressure of cadmium. Since over the temperature range investigated the cadmium pressure over cadmium-saturated CdSe is very close to that over pure liquid cadmium, the carrier concentrations plotted are expected to be within a few percent of the concentrations at the cadmium-rich solidus of CdSe. Along the solidus the cadmium concentration in excess of the stoichiometric composition of CdSe is onc-half the carrier concentration shown, for example, 1.1×10^{18} cm^{-3} at 900°C.

F. T. J. Smith

E. GERMANATES AND STANNATES WITH THE $PbSb_2O_6$ STRUCTURE

Magneli[22] has determined the crystal structure of $PbSb_2O_6$. It consists of a hexagonal closc-packed array having alternate basal planes of octahedral interstices 2/3 filled by Sb^{5+} ions and interleaved plancs of octahedral sites 1/3 filled with Pb^{2+} ions. The cations ordcr within the planes, with the Sb^{5+} ions forming a simple-hcxagonal array having Pb^{2+} ions at the body-center of each hexagonal prism of Sb^{5+} ions. A variety of antimonates $M^{II}Sb_2O_6$ (M^{II} = Ba, Sr, Ca, Hg, Co, Pb) (Ref. 22) and arsenates $M^{II}As_2O_6$ (M^{II} = Sr, Ca, Hg, Cd, Pb, Co, Ni) (Refs. 22, 23) have been prepared with this structure. Morc recently compounds with similar structure have been prepared in which one or both of the Sb ions have been replaced by other cations: $LaTiSbO_6$ and $LaTi_{1.5}W_{0.5}O_6$ (Ref. 24), $LnCrTeO_6$ (Ln = La, . . . Yb) (Ref. 25), and $M^{II}TiTeO_6$ (M^{II} = Ca, Sr, Ba) (Ref. 26). Thc investigation reported here is primarily concerned with some new germanium and tin compounds with $PbSb_2O_6$ structure.

The compounds listed in Table II-3 have been prepared from stoichiometric amounts of rare earth oxides, alkaline earth and Mn carbonates, GeO_2, SnO_2 and TiO_2 by a sintering procedure described previously[27,28]. Table II-3 givcs the hexagonal lattice constants, sintering

TABLE II-3

LATTICE CONSTANTS, SINTERING TEMPERATURE AND TIME, AND COLOR OF SOME COMPOUNDS WITH $PbSb_2O_6$ STRUCTURE

Compound	o (Å)	c (Å)	Sintering Temperoture (°C)	Sintering Time (h)	Color
$MnGeTeO_6$	4.999	4.678	750	1	brown red
$CoGeTeO_6$	5.034	5.060	950	1	white
$SrGeTeO_6$	5.066	5.402	850	1	light pink
$BoGeTeO_6$	5.096	5.791	800	1	light yellow
$LoGeSbO_6$	5.117	5.218	1250	1/2	white
$PrGeSbO_6$	5.106	5.121	1050	1	light grey
$NdGeSbO_6$	5.097	5.086	1050	5	light violet
$SmGeSbO_6$	5.088	5.027	1050	1	white
$EuGeSbO_6$	5.085	4.996	1100	2	white
$GdGeSbO_6$	5.081	4.969	1080	5	white
$TbGeSbO_6$	5.075	4.938	1100	1	light beige
$DyGeSbO_6$	5.071	4.907	1050	1	light yellow
$HoGeSbO_6$	5.068	4.881	1050	1	light oronge
$ErGeSbO_6$	5.063	4.855	1100	10	pink
$TmGeSbO_6$	5.060	4.825	1100	2	light yellow
$YbGeSbO_6$	5.055	4.805	1100	10	light yellow
$LuGeSbO_6$	5.054	4.776	1100	1	light yellow
$YGeSbO_6$	5.065	4.879	1100	1	white
$BoSnTeO_6$	5.332	5.729	950	1	white
$SrSnTeO_6$	5.301	5.303	850	1	white
$LoSnSbO_6$	5.324	5.190	1300	1/6	white
$PrSnSbO_6$	5.311	5.091	1250	1	light green
$NdSnSbO_6$	5.307	5.058	1300	1	light blue
$Nd_2Ti_3TeO_{12}$	5.141	5.040	1000	1	light blue
$LoTiSbO_6$	5.209	5.174	1250	1	white
$PrTiSbO_6$	5.197	5.081	1200	1	light grey
$NdTiSbO_6$	5.192	5.051	1200	1	light blue
$SmTiSbO_6$	5.181	4.989	1200	1/4	light yellow
$EuTiSbO_6$	5.177	4.960	1200	1/4	white

temperature and time, and color for each material. X-ray powder patterns were obtained with Mn-filtered iron radiation, using a camera of 360-mm circumference. In contrast with the $LnCrTeO_6$ compounds, the powder patterns do not show superstructure lines. However it is very probable that the cations Ge-Te, Ge-Sb, Sn-Te, Sn-Sb and Ti-Sb are ordered with unlike near neighbors in each basal plane, and that there is also some short range order between these cation planes. For the heavier rare earth-germanium antimonates (Er, Tm, Yb, Lu) the x-ray patterns indicated the presence of a small quantity of a second phase.

In the $LnGeSbO_6$ series, as in the $LnCrTeO_6$ series, the dependence on the radius of the rare earth ion is greater for the c parameter than for the a parameter (Fig. II-13). This behavior is characteristic of a layer structure. For a particular $LnCrTeO_6$ compound, the a parameter is always larger and the reduced c parameter always smaller than for the corresponding $LnGeSbO_6$ compound. This indicates that the O-GeSb-O layers are slightly contracted relative to the O-CrTe-O layers and that the rare earth ion moves slightly away from the negatively charged triple layers. An even greater increase in the a parameter and reduction in the c parameter occurs when Ge in $BaGeTeO_6$ is replaced by Sn.

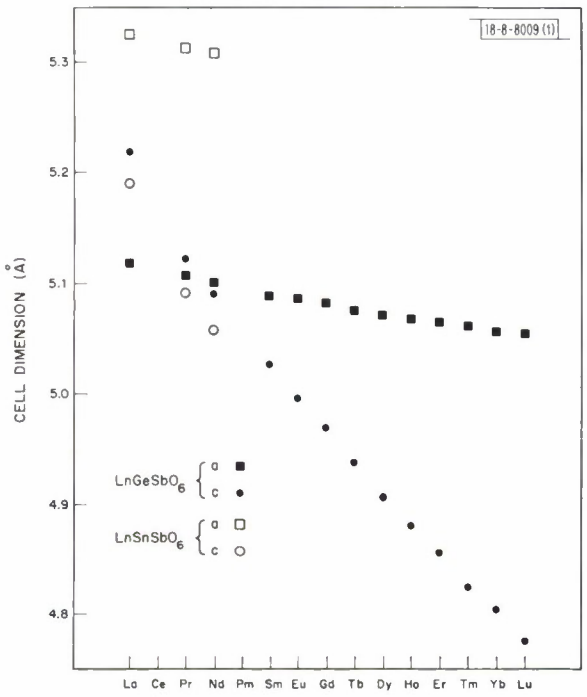

Fig. II-13. Cell dimensions a and c for $LnMSbO_6$ compounds (M = Ge, Sn).

Optical studies of mixed oxides of transition metals lead to the conclusion that the main group cations (e.g., Sn, As, Sb, Te) generally coordinate the surrounding oxygen ions in a regular octahedron, whereas the transition elements (e.g., Ti, Nb, Ta, W) in their highest oxidation state tend to bond the oxygen ions in a distorted octahedron.[29] It has also been concluded that the main group cations cause a higher degree of covalency in the bond between oxygen and the other cation. These characteristics are consistent with the formation of an extended series of Ge^{4+} and Sn^{4+} compounds with $PbSb_2O_6$ structure despite some mismatch between the radii of these main group ions and those of Sb^{5+} and Te^{6+}.

Compounds with the $PbSb_2O_6$ structure can be formed when the ionic radius of the ion in the larger site is about two to three times as large as those of the cations in the small octahedra. If all cations are of about equal size, then the rutile structure occurs.

The colors of the rare earth compounds listed in Table II-3 correspond closely to those of their rare earth cations in aqueous solution. Although Mn^{2+} ions generally give light colors, $MnGeTeO_6$ is red-brown. This color is probably due to the presence of Mn^{4+}, small amounts of which are known to give rise to red colors. For example, Al_2O_3 containing 2 mol percent Mn is dark purple[30] and $MgTiO_3$ with 0.2 mol percent Mn is rose violet.[31] The formation of Mn^{4+} takes place at 700 °C for $MgTiO_3$:Mn and at 600 °C for Mg_2TiO_4:Mn. These temperatures are

close to the preparation temperature of $MnGeTeO_6$ (750°C). The diffuse reflectance spectrum of this compound measured in our laboratory at about 10°K (Fig. II-14) shows absorption peaks at 14150 cm^{-1} and 14650 cm^{-1} which can be assigned to the spin forbidden transitions $^4A_2 \rightarrow {}^2E$ and $^4A_2 \rightarrow {}^2T_{1g}$, respectively, of Mn^{4+}. An absorption at about 18000 cm^{-1} is probably due to the transitions $^4A_2 \rightarrow {}^4T_{1g}$ of Mn^{4+} and $^6S \rightarrow {}^4T_{1g}$ of Mn^{2+}. At 4.2K a weak fluorescence line was observed at 12000 cm^{-1}.

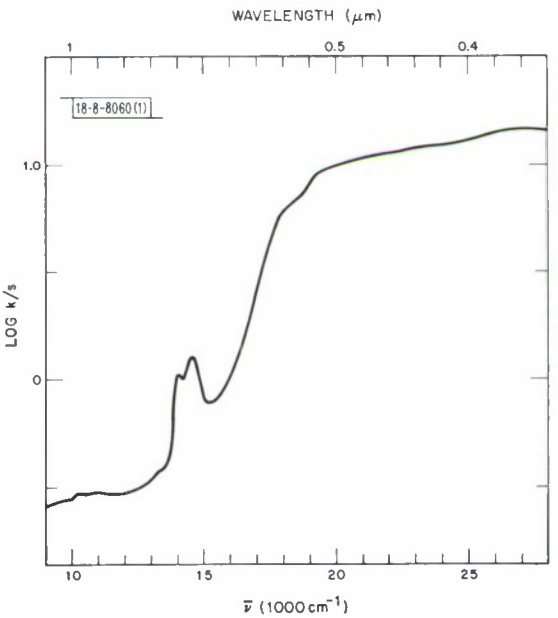

Fig. II-14. Diffuse reflectance of $MnGeTeO_6$ at 10°K. The quantity k/s is equal to $(1-R)^2/2R$, where k is absorption coefficient, s is a scattering coefficient, and R is measured reflectance of the sample relative to reflectance of a CaF_2 standard.

It is concluded that under the present preparation conditions a small amount of Mn^{4+} substitutes for Ge^{4+} in $MnGeTeO_6$. This is not surprising since the ionic size and the electron configuration t_{2g}^3 of Mn^{4+} are expected to give a good fit with the octahedral sites in the O-GeTe-O layers.

H. M. Kasper

F. OXIDES WITH THE Na_2SiF_6 STRUCTURE

Brandt[32] has reported that $MnSb_2O_6$, which he prepared by reacting Mn with Sb_2O_3 at 1000°C for 24 hours, probably has the orthorhombic niobite structure. A subsequent investigation[33] of other antimonates containing transition metal cations failed to reveal any with this structure. The unique position of $MnSb_2O_6$ has prompted a re-determination of its structure.

The compound, a yellow powder, was prepared from a stoichiometric mixture of $MnCO_3$ and Sb_2O_3, which was slowly heated in air to 1000°C and kept at this temperature for 24 hours. An x-ray powder pattern was obtained with Mn-filtered Fe radiation. The pattern failed to confirm the niobite structure, but could be indexed on a hexagonal cell with a = 8.795 Å and c = 4.718 Å. The possibility that the structure is closely related to that of Na_2SiF_6 (a = 8.859, c = 5.038; see Ref. 34) was suggested by the similarity in hexagonal lattice dimensions and by the fact that all the cations in Na_2SiF_6 occupy octahedral sites, as is expected for $MnSb_2O_6$.

This identification was confirmed by the similarity in the relative intensities of the x-ray diffraction lines. Intensity calculations have now shown that Mn occupies one of the two types of Na sites (e) and that Sb occupies the other type (f) as well as both types of Si sites (a, d).

We have also prepared two new compounds, $MnSnTeO_6$ and $MnTiTeO_6$, in which the Sb_2 ions in $MnSb_2O_6$ are replaced by SnTe and TiTe, respectively. From the similarity of their diffraction patterns and lattice parameters (see Table II-4) to those of $MnSb_2O_6$, it is concluded that

TABLE II-4

LATTICE CONSTANTS OF COMPOUNDS WITH Na_2SiF_6-RELATED STRUCTURES*

Compound	a (Å)	c (Å)
$K_2S_2O_6$ (Ref. 36)	9.785	6.295
Na_2SiF_6 (Ref. 34)	8.859	5.038
$MnSb_2O_6$	8.802	4.719
$MnTiTeO_6$	8.632	4.728
$MnSnTeO_6$	8.781	5.049
Lu_2TeO_6	8.947	5.071
In_2TeO_6	8.880	4.820
Sc_2TeO_6 (Ref. 35)	8.74	4.80

* Determined in this study unless otherwise noted.

these compounds also have structures related to the Na_2SiF_6 structure. The same conclusion can be drawn concerning the tellurates Lu_2TeO_6, In_2TeO_6, and Sc_2TeO_6 (Ref. 35). Intensity calculations for these compounds show that Lu, In, or Sc occupy both Na sites, and Te occupies the two Si sites.

H. M. Kasper

G. RELATIONSHIP OF STRUCTURE TO PHYSICAL PROPERTIES OF THE $M_xV_2O_5$-β PHASES

The $Na_{0.33}V_2O_5$-β structure of Fig. II-15, which was originally determined by Wadsley,[37] has been re-examined to demonstrate how the detailed atomic positions provide important information about the physical properties.

In the Wadsley phase, the M^+ ions occupy randomly M_1, M_1' positions within the tunnels. The M_1-M_1' separation in an a-c plane is only ≈ 1.95 Å, which prohibits simultaneous occupancy of these sites. Therefore the maximum value of x for the $M_xV_2O_5$-β phase should be x = 0.33. Nevertheless the $M_x^+V_2O_5$ systems having smaller M^+ ions ($M^+ = Cu^+$, Li^+, Hg^+, Na^+) have been reported to have the β phase extending to $x > 0.33$. A re-examination[38] of the powder data on $Li_xV_2O_5$ has revealed the existence of two phases: a Wadsley β phase in the range

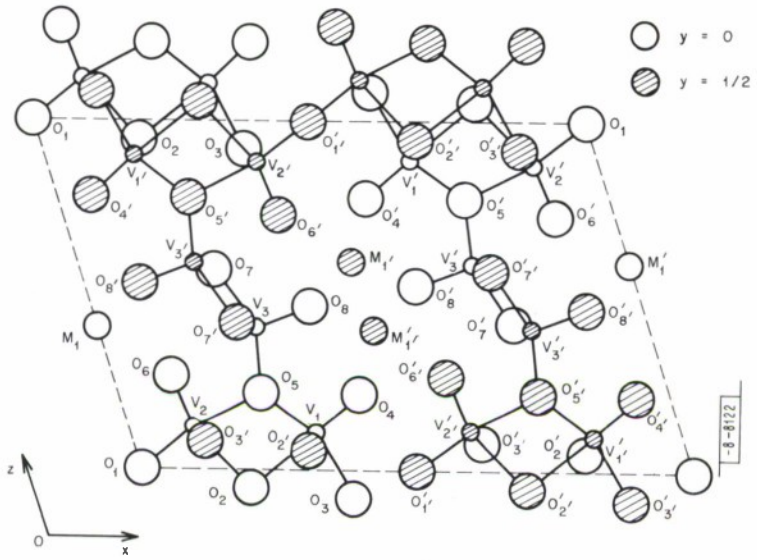

Fig. II-15. Wadsley $No_xV_2O_5$-β phose projected on an a-c plone. Sites M_1, M'_1, $M_{1'}$, and $M'_{1'}$ are "randamly" occupied by No^+ ions, althaugh two neighboring sites in some tunnel ond a-c plone connat be accupied simultaneously.

$0.22 \leqslant x \leqslant 0.37$ and a β' phase in the range $0.44 \leqslant x \leqslant 0.49$. A single-crystal study[39] of the β' phase has shown that the vanadium-oxygen array is essentially the same as in the β phase, but the Li^+ ions occupy tetrahedral sites within the tunnels rather than the M_1 sites. These interstitial positions are designated M_3, M'_3 in Fig. II-16. For the larger cations $M^+ = Na^+$ and Ag^+; on the other hand, the maximum x is $x_f = 0.40$ and 0.41, and a single-crystal study[40] of $Na_{0.4}V_{1.6}Mo_{0.4}O_5$ indicates that the excess Na^+ ions occupy interstitial positions M_2, M'_2 of

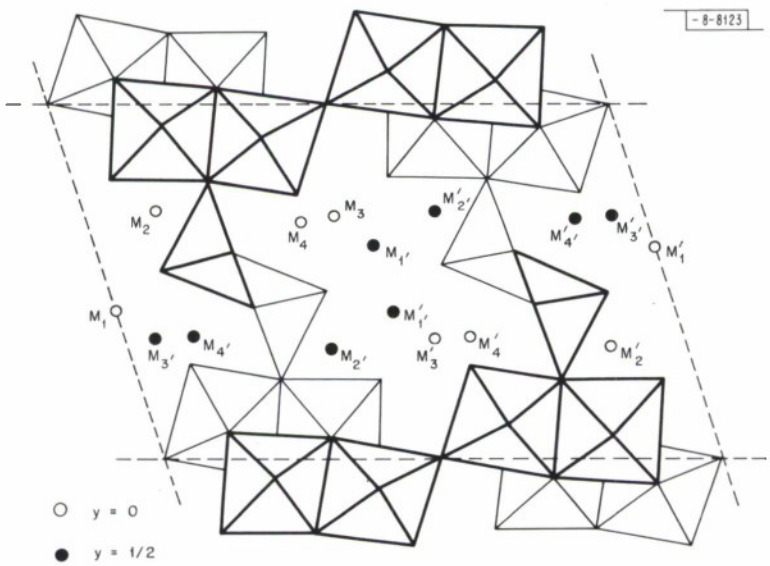

Fig. II-16. Definitions of possible tunnel sites for M^+ ians in o $M_xV_2O_5$-β phose.

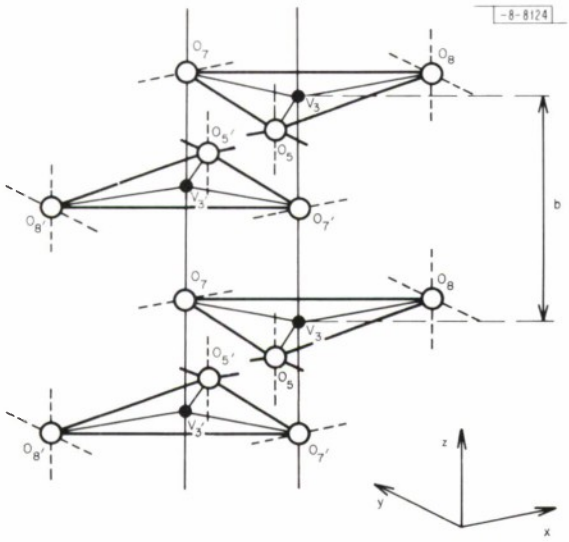

Fig. II-17. Idealized bipyramidal-site chain parallel to b axis in a $M_xV_2O_5$-β phase.

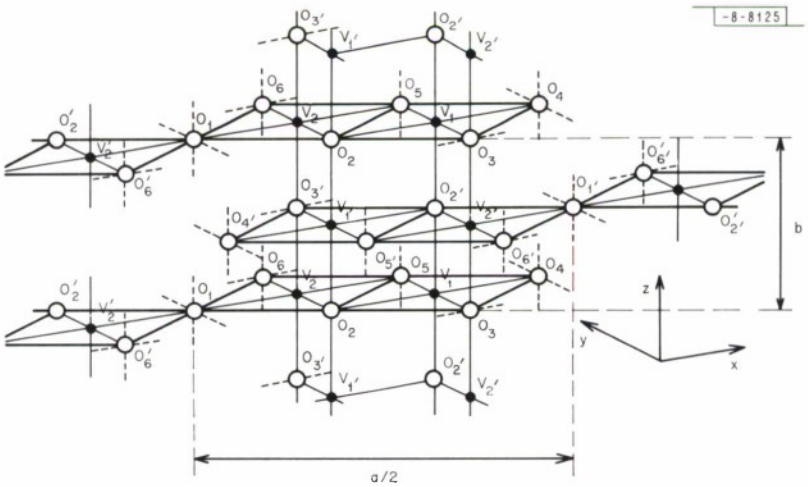

Fig. 18. Idealized octahedral-site chain parallel to the b axis in a $M_xV_2O_5$-β phase.

Fig. II-16. In the phases $Na_xV_2O_5$-β and $Ag_xV_2O_5$-β, discontinuities in the effective paramagnetic moment μ_{eff} vs composition x have been observed,[40,41] indicating that there is a cooperative displacement of the M^+ ions into the interstitial tunnel sites M_2 at $x > 0.33$. Since no such discontinuities were observed in the system $Cu_xV_2O_5$ over the entire range $0.26 \leqslant x \leqslant 0.64$, it was suspected that this is a β' phase, like the Li^+-rich $Li_xV_2O_5$-β' phase. Subsequent x-ray analysis[40] has shown that this conjecture is essentially correct. However, a small distortion is superimposed that lowers the symmetry.

Measurements of electrical conductivity[40-43] have shown that resistivities parallel to the tunnel axis are three orders of magnitude smaller than those perpendicular to the tunnel axis. Contrary to earlier assumptions,[42] it is now clear that the M^+ ions are ionized, donating their outer electron to the V_2O_5 array. Further, there is considerable evidence that the d-like electrons in these arrays are small polarons with an activation energy for electrical conduction in the range 0.02 to 0.05 eV. However, the variation of the Seebeck coefficient with x could not be interpreted with the conventional small-polaron formula and straightforward statistics,[41,44] so it is necessary to inquire about the distribution of the V^{4+} ions in the structure.

Figures II-17 and II-18 show idealized bipyramidal-site and octahedral-site chains running parallel to the tunnel axis. They represent, respectively, the V_3 subarray and the two interpenetrating V_1 and V_2 arrays. The dashed lines represent anion p_π orbitals available for bonding with vanadium d orbitals in the absence of M^+ ions. The cationic and anionic sites are labeled as in Fig. II-15. The oxygen p orbitals not active in σ bonding are represented by the dashed lines in these two figures. These are necessarily active in π bonding with the vanadium ions. Displacements of the vanadium ions from the center of symmetry of their respective interstices is caused by two cooperative forces: electrostatic cation-cation repulsive forces and unequal cation-anion interactions as a result of different π-bond contributions from the different anions. The shortest cation-anion separations are V_3-O_8 = V_1-O_4 = 1.57 Å and V_2-O_6 = 1.60 Å, where there are two π-bonding orbitals on the anion. The V_2-O_1 = 1.81 Å bond is not a triple bond, even though there are two π-bonding p orbitals per O_1 ion, because the O_1-ion π-bonding orbitals are shared by two V_2 atoms on opposite sides. From such reasoning it follows that in the vanadium oxides bond lengths are reliable indicators of the multiplicity of the cation-anion bonding:

Triple bonds have V^{5+}-$O^{2-} \leqslant 1.60$ Å

Double bonds have V^{5+}-$O^{2-} \simeq 1.80$ Å

Single bonds have V^{5+}-$O^{2-} \geqslant 1.89$ Å

An important conclusion is that, since the V_3-O_5 = 1.82 Å separation is close to that for a double bond whereas the V_1-O_5 = 1.95 Å separation is larger than that for a single V^{5+}-O^{2-} bond, the O_5-ion π-bonding orbital bonds primarily with the V_3 ion. Further, since the d orbitals are antibonding with respect to the anion array, the stronger the d orbital participation in bonding, the less stable the crystal-field d-like orbital. Therefore, from a consideration of the bond distances, it is possible to conclude unambiguously that the ground state for the mobile electrons in the β-phase structure is a localized d_{zy} orbital at a V_1 site. In addition, since 180° V^{5+}-O^{2-}-V^{5+} interactions are strong enough to form collective d-like orbitals whenever two π-bonding p orbitals are available at the intermediary anion,[45] the V_2-O_1-V_2' configurations should be considered as single molecular units characterized by molecular rather than atomic

orbitals. Therefore the small polaron at a V_1 site will jump to a pair of V_2 sites, which reduces the number of countable sites for electron hopping. The Seebeck coefficient for a small polaron semiconductor is

$$\alpha = A - 198 \log[(N - x)/x]$$

where the transport term A is of order unity and N is the total number of sites per formula unit available to the small polarons. To account for the V_2-O_1-V_2' pairs as molecular units, N is reduced from 2 to 5/3. If this concept is extended to the assumption that each M^+ ion perturbs the V_2O_5 array so as also to eliminate one countable site by creating a molecular orbital at a pair or cluster, then

$$N = \frac{2}{3}(n_1 + n_2 + n_3) = \frac{5}{3} - \frac{2}{3}x$$

when the n_i are the numbers of available sites per formula unit on sublatticcs V_1, V_2 and V_3. Since A can generally be neglected for small-polaron oxides, the Seebeck coefficient becomes

$$x = -198 \log[(5/3)(1 - x)/x] \quad . \tag{II-1}$$

This expression, which contains no adjustable parameters, is shown as the full curve in Fig. II-19. From a consideration of the various bond lengths in the structure, it is anticipated that the molecular units created by M^+-ion perturbations are V_3-O_7'-V_3 units.

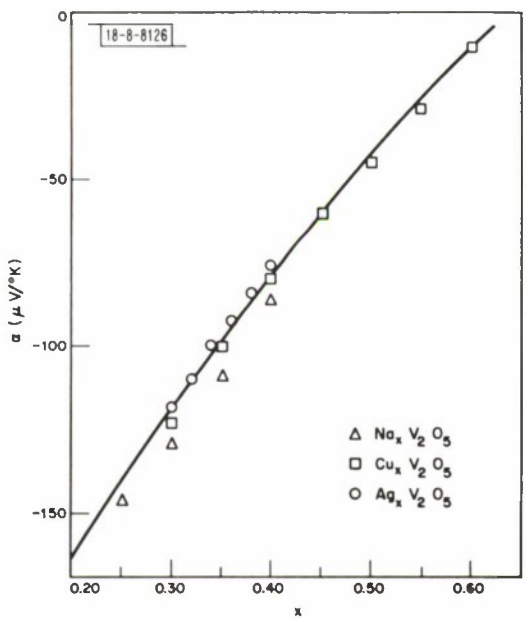

Fig. II-19. Room temperature Seebeck coefficient vs M^+ concentration (x) in $M_xV_2O_5$-β phases [experimental points from Refs. 40 and 41, theoretical curve from Eq. (II-1) in text].

This analysis is supported by several additional experimental findings: (a) In the system $Na_xV_{2-x}Mo_xO_5$-β, the Mo atoms all go into V_2 positions, if $x \leqslant 0.33$, but for $x > 0.33$ the V_2 positions contain 1/2 Mo + 1/2 V, presumably in Mo^{6+}-O_1-V^{4+} units, and the excess (x − 0.33) Mo atoms per formula unit occupy V_3 positions.[46] It may be assumed that a Mo^{6+} ion would not substitute on a V^{4+}-ion position. (b) Variation with x of the activation energy for electron hopping and of the magnetic susceptibility per small polaron extrapolate to collective-electron orbitals of a V_3-O_7' array overlapping the energy of the d_{yz} orbitals at V_1 sites for larger values of x. (c) The V_1-V_1' separation is too large for a small activation energy for conduction within the V_1 sublattice, but the large anisotropy for conductivity would also be consistent with conduction via the V_3-O_7' array, and a small activation may be associated with a shift of an O_5 ion from $V_1 \ldots O_5$-V_3 to V_1-$O_5 \ldots V_3$.

This work was done while visiting the group of Prof. Paul Hagenmuller at the University of Bordeaux, and it was made possible only through collaborative discussion of their unpublished experimental data.

J. B. Goodenough

H. ABSOLUTE MEASUREMENT OF THE ATOMIC FORM FACTOR OF Ni

The accurate measurement of x-ray structure factors on an absolute scale provides an extremely useful check on current solid state models. In the case of Ni, for instance, magnetic moment measurements suggest that the number of d electrons is 9.4 instead of 8 as in the free atom ground state. In other words, the effect of the crystal field is to give a d character to 1.4 s electrons. This should affect the charge distribution in the solid and hence the x-ray structure factors.

There have been two recent x-ray measurements[47,48] on Ni of sufficient accuracy to warrant comparison with theory. Inkinen and Suortti[47] (IS) measured the first 30 reflections on powder using filtered MoK_α radiation, while Diana, Mazzone, and DeMarco[48] (DM) measured, on an absolute scale, six structure factors by transmission through thin single crystals. For the sake of comparison, the IS results have been readjusted using the best recent values of $\Delta f'$ (Ref. 49) and μ (Refs. 50 through 53) and are presented in Table II-5 together with the DM values and the $3d^8 4s^2$ relativistic Hartree-Fock form-factors (RHF) of Doyle and Turner.[54] As can be seen, there is a strong disagreement between these workers on all reflections except the (511,333), DM being consistently lower than IS. With respect to RHF, the IS values are close for all peaks except the first three which are high, while the DM results are low for all peaks.

TABLE II-5
SCATTERING FACTORS OF NICKEL

hkl	$\frac{\sin\Theta}{\lambda}$ ($\AA^{-1}$)	Inkinen and Suortti[47] (powder)	Diana, et al.[48] (single crystals)	This Work (powder)	Theory[54] (Relativistic Hartree-Fock)
111	0.2458	20.64 ± 0.13	20.10 ± 0.13	20.00 ± 0.18	20.54
200	0.2838	19.46 ± 0.07	18.55 ± 0.16	18.81 ± 0.18	19.25
220	0.4013	15.67 ± 0.03	15.34 ± 0.12	15.37 ± 0.15	15.54
400	0.5676	11.50 ± 0.11	11.18 ± 0.11		11.58
511	0.7373	8.88 ± 0.05	8.73 ± 0.09		8.99
333	0.7373	8.88 ± 0.05	8.74 ± 0.09		8.99

In an attempt to resolve this discrepancy, we have measured on an absolute scale the first three structure factors of Ni using monochromatic CuK_α radiation. The experimental procedure used has been described previously.[55] The monochromator constant was measured to be 0.780 ± 0.016. The mass absorption coefficient of Ni was measured on foils whose purity was checked by mass spectrometry. It was found to be 49.0 ± 0.4 cm^2/g, in good agreement with published values,[50-53] whose average is 48.94 ± 0.3 cm^2/g. The samples were pellets pressed from Ni sponge of 4 μ average particle size. The effects of preferred orientation, primary extinction, surface roughness and porosity were checked by measuring samples formed at pressures varying from 5 to 60 kpsi.

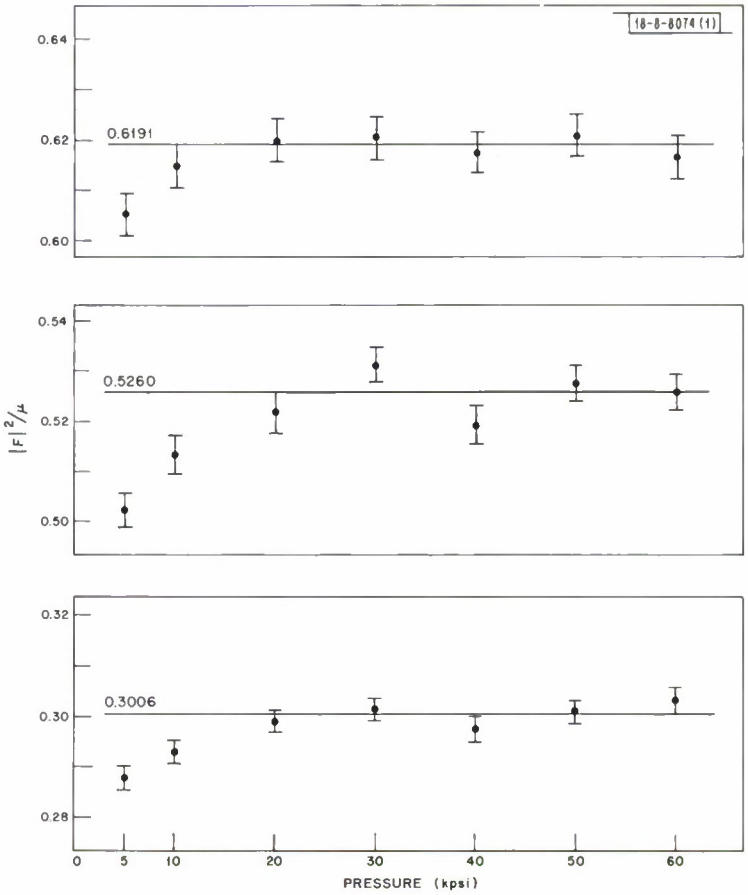

Fig. II-20. Measured structure factors for Ni as a function of pressure used to form samples.

The measured values of $|F(hkl)|^2/\mu$, where F is the structure factor for Miller indices hkl and μ is the linear absorption coefficient ($= 436\ cm^{-1}$ for Ni), are plotted in Fig. II-20 against the pressure used to form the samples. The figure shows that samples formed between 20 and 60 kpsi give consistent values which have been averaged to obtain the adopted values of $|F(hkl)|^2/\mu$. The form factors were obtained from these values by using the expression $F(hkl) = [f^\circ(s) + \Delta f' + i\Delta f'']\exp[-Bs^2]$, where $s = \sin\theta/\lambda$, θ is the Bragg angle, λ is the x-ray wavelength, $f^\circ(s)$ is the form factor, $\Delta f'$ and $\Delta f''$ are the real and imaginary parts of the anomalous dispersion correction, and B is the Debye-Waller factor. In making the calculations, we used the value $\Delta f' = -3.2$, which was obtained by integrating the experimental mass absorption coefficient over the suitable wavelength range. It agrees with the value given by Cromer.[49] The other values used are $\Delta f'' = 0.67$ and $B = 0.381 \pm 0.008$. The latter was obtained from neutron inelastic scattering measurements.[56]

The form factors obtained from our data are listed in Column 5 of Table II-5. Within the error of experiment, they agree with the values of Diana, et al.,[48] but not with those of Inkinen and Suortti.[47]

P. M. Raccah
V. E. Henrich

I. HIGH PRESSURE FORMS OF Cd_3As_2 AND Zn_3As_2

Pressure-temperature phase diagrams of Zn_3As_2 and Cd_3As_2 (Fig. II-21) have been proposed by Jayaraman, Anantharaman and Klement[57] on the basis of an interpretation of their DTA data at high temperature and pressure. They suggested that the high pressure phases of Zn_3As_2 and Cd_3As_2 would have the trigonal $P\bar{3}ml$ structure.

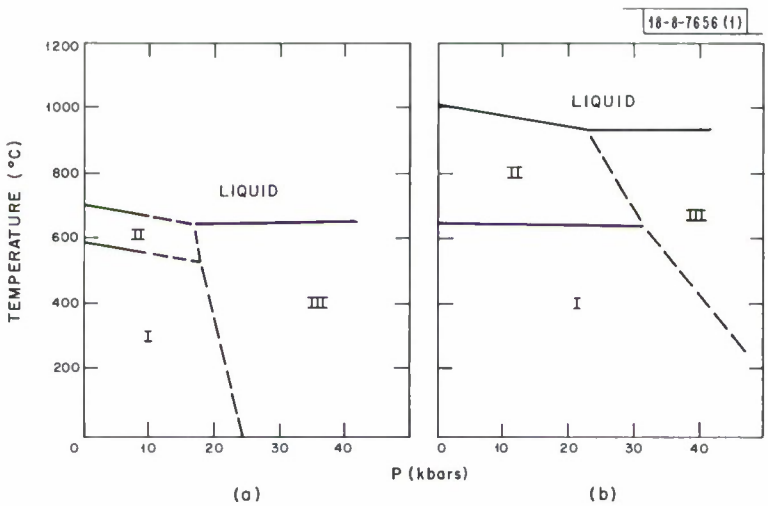

Fig. II-21. Phase diagrams prapased by Jayaraman, Anantharaman, and Klement.[57] Datted lines indicate baundaries with na data paints. (a) Cd_3As_2 (phase I-III baundary drawn ta carrespand ta resistance break abserved at 24 kbars and raam temperature). (b) Zn_3As_2.

Recently Katzman, Donohue and Libby[58] reported confirmation of the proposed trigonal structure, with $a_o = 4.30$ Å, $c_o = 6.87$ Å, and $c/a = 1.60$, by x-ray diffraction patterns taken on high prcssurc samples retained at liquid nitrogen temperature. No tabulation of diffraction data was included in their paper.

We have studied the effect of pressure on the structures of Cd_3As_2 and Zn_3As_2 by means of measurements at room temperature in diamond anvil x-ray diffraction cameras from atmospheric pressure to ~140 kbars. Both compounds transform at high pressures to structures which we have indexed as trigonal but which have cell dimensions about twice the size of those reported by Katzman, et al.[58] for Cd_3As_2. In addition, the data suggest the possible existence of cubic intermediate phases. We have also obtained diffraction patterns at 110°K and atmospheric pressure on samples of Cd_3As_2 quenched from high pressure. The results for the various samples are similar and in essential agreement with the trigonal high pressure structure determined from the x-ray pressure camera data.

The Zn_3As_2 and Cd_3As_2 were prepared by reacting the metal and arsenic in an open-tube vertical reactor,[59] and then purifying the product by forced convection vapor crystal growth.[60] Metallographic examination of polished sections showed no second phase inclusions. The tetragonal structures and lattice parameters agree with those reported for Cd_3As_2 (Rcf. 61) and for Zn_3As_2 (Rcf. 62). The densities of the crystals, measured by toluene displacement, are in

excellent agreement with the calculated x-ray densities (Cd_3As_2, 6.29 g/cc measured and 6.28 g/cc calculated;[61] Zn_3As_2, 5.57 g/cc measured and 5.60 g/cc calculated).

The high pressure x-ray studies employed two types of diamond-anvil squeezers using Mo radiation with a Zr filter. One type is pressurized by N_2 gas,[63] and the other employs screw loading of the diamonds.[64]

Low temperature diffractometer runs were made on three Cd_3As_2 samples. Two were annealed at 600°C and 40 kbars for 24 hours, then quenched to liquid nitrogen temperature before releasing the pressure. A third sample was annealed at 1000°C and 30 kbars for 3 hours, cooled slowly over 4 hours to room temperature, held overnight, then quenched to liquid nitrogen temperature before releasing the pressure. Diffractometer patterns on specimens from each run were obtained at 110° ± 5°K and atmospheric pressure, using CuKα radiation.

Low temperature diffractometer runs were also made on two Zn_3As_2 samples. One was annealed at 65 kbars for 30 minutes at 1000°C and then for 2 1/2 hours at 600°C, after which it was quenched to liquid nitrogen before releasing the pressure. The second was annealed at 60 kbars for 15 minutes at 1000°C and for 2 hours at 700°C, then quenched to liquid nitrogen before release of pressure.

The x-ray patterns of Cd_3As_2 at pressures below ~25 kbars show only the lines of the tetragonal phase. Above this pressure, lines of a high pressure phase appear. At pressures greater than 40 kbars only the lines of this high pressure phase are obtained. The d-spacings observed in a pattern obtained with the gas-loaded camera at 55 kbars are listed in Table II-6. The pattern is indexed on a trigonal structure with the parameters a_o = 7.94 Å, c_o = 12.82 Å, and c/a = 1.61. The d-spacings calculated from these parameters, which are given in Table II-6, agree quite well with the observed values. The calculated density is 6.9 g/cc, an increase of ~10 percent over the tetragonal phase at atmospheric pressure. Table II-6 also lists the d-spacings calculated from the parameters given by Katzman, et al.[58] for their retained phase. The data show that the strong lines obtained at 55 kbars cannot be indexed by using Katzman's parameters.

The x-ray patterns for Zn_3As_2 at pressures above ~70 kbars are similar to those obtained for the high pressure trigonal phase of Cd_3As_2. The d-spacings observed in patterns obtained at an estimated 55 kbars and an estimated 70 kbars are listed in Table II-7. The pattern obtained at ~70 kbars is indexed on a trigonal structure, with a_o = 7.27 Å, c_o = 12.08 Å and c/a = 1.66. As in the case of trigonal Cd_3As_2, the agreement between calculated and observed d-values is quite good. The calculated density is 6.2 g/cc, an increase of 11 percent over the tetragonal phase at one atmosphere. The pattern at ~55 kbars cannot be indexed as either tetragonal or trigonal. This pattern can be indexed, with very good d-values, on an fcc cell with a_o = 11.82 Å. However, the assignment of this structure is somewhat questionable, since within experimental error the calculated density for the fcc phase is the same as the density of the atmospheric pressure phase. Furthermore, no fcc structure has been reported for the A_3B_2 compounds.

The volume compressibilities of the tetragonal and trigonal phases of Cd_3As_2 and Zn_3As_2 were determined from x-ray pressure camera data and are listed in Table II-8.

The lines observed in the diffractometer patterns for Cd_3As_2 retained at low temperatures could all be accounted for by the trigonal high pressure structure determined from the x-ray pressure camera work (Table II-6). For Zn_3As_2, however, the low temperature diffractometer patterns could not be indexed completely on any single known phase. However, the major phase did appear to be the atmospheric pressure phase.

TABLE II-6

OBSERVED AND CALCULATED d-SPACINGS FOR HIGH PRESSURE TRIGONAL PHASE OF Cd_3As_2

From Diffroction Pattern at ~55 kbars				From Porameters Reported for Retoined Phose	
Intensity (obs)	d(obs)	d(colc)*	hkl	d(colc)†	hkl
< 0.5	3.415	3.435	20.0	3.435	00.2
< 0.5	3.205	3.204	00.4	3.271	10.1
0.5	3.028	3.025	20.2		
10	2.851	2.901	10.4		
4	2.707	2.679	20.3		
< 0.5	2.469	2.494	11.4	2.519	10.2
5	2.236	2.220	21.3		
8	2.015	2.018	21.4		
4	1.862	1.865	30.4	1.863	20.0
1 (diffuse)	1.720	1.720	40.0	1.720	00.4
0.5	1.513	1.515	40.4		
0.5	1.426	1.425	00.9	1.408	21.0
1	1.312	1.313	30.8	1.303	21.2
1	1.232	1.232	51.1	1.222	30.1

* Colculated from o_o = 7.94 Å, c_o = 12.82 Å.

† Katzman, et al.[58] give o_o = 4.30 Å, c_o = 6.87 Å. No line positions or intensities ore given.

An important problem in the study of high pressure-temperature phase diagrams is whether or not measurements on a retained phase yield reliable information concerning the phase in equilibrium at the pressure and temperature from which the retained phase was quenched. This problem is emphasized by the difference between the trigonal structure reported by Katzman, et al.[58] for retained Cd_3As_2 and the trigonal structure we observed above 40 kbars. There are three possible explanations for the difference in the apparent cell dimensions. First, the phase retained by Katzman might not have been an equilibrium phase but one which occurred only on the release of pressure. This seems unlikely, since the retained phases of Si, Ge, and InSb (including the β-Sn phase) have all been shown to be equilibrium phases in their P-T diagrams. Second, since the retained phase had been heated to 1000°C at 30 kbars and then slowly cooled through the phase III region (Fig. II-21), it might have been an additional high pressure phase stable at high temperature. Finally, the retained phase might actually be the same as the phase observed at high pressure but the structure deduced may be different because of factors affecting the diffraction patterns, as described below. Since our efforts to duplicate the Katzman results

TABLE II-7

OBSERVED AND CALCULATED d-SPACINGS FOR HIGH PRESSURE PHASES OF Zn_3As_2

Trigonol Phose (est. 70 kbors)				FCC Phose (est. 55 kbors)			
Intensity (obs)	d(obs)	d(colc)*	hkl	Intensity (obs)	d(obs)	d(colc)†	hkl
1	3.319	3.388	10.3	10	3.417	3.419	222
4	3.157	3.153	20.0	0.5	2.988	2.961	400
10	2.644	2.702	11.3	2	2.726	2.717	331
3	2.514	2.482	20.3	8	2.097	2.090	440
5	2.078	2.052	21.3	5	1.791	1.783	622
10	1.873	1.865	30.3	2	1.478	1.479	800
5	1.726	1.728	00.7	2	1.358	1.358	662
0.5	1.615	1.622	31.3	0.5	1.309	1.299	911
0.5	1.314	1.313	10.9	4	1.205	1.208	844
1	1.218	1.218	33.0	1	1.146	1.139	1022
1	1.144	1.143	42.3				

* Colculoted from o_o = 7.27 Å, c_o = 12.08 Å.

† Colculoted from o_o = 11.82 Å.

TABLE II-8

VOLUME COMPRESSIBILITIES OF SOME PHASES OF Zn_3As_2 AND Cd_3As_2

Compound	Phose	Pressure Ronge	$-\frac{\Delta V}{V_o \Delta p}$ (kbor^{-1})
Cd_3As_2	Tetrogonol	Atm to 15 kbors*	2×10^{-3}
	Trigonal	55† to 133 kbors*	6×10^{-4}
Zn_3As_2	Tetrogonol	Atm to 23 kbors*	1×10^{-3}
	Trigonol	80* to 138 kbors*	5×10^{-4}

* NoCl internol colibront.

† Estimoted from lood-pressure colibrotion with NoCl.

on retained phases verified the trigonal structure we determined from the high pressure camera results, it would seem the final explanation probably applies in the case of Cd_3As_2.

We found in studies on retained InSb phases that samples which had been heated at pressure had preferred orientations which resulted in much diminished intensities for some reflections and increased intensities for others in low temperature (100°K) diffraction patterns.[65,66] In addition, the internal strain present in quenched samples caused considerable broadening of the peaks and a high background from which weak peaks could not be resolved. In the case of InSb III, the sample retained from 30 kbars and 350°C gave a very poor hexagonal pattern. Only after indexing was accomplished from the better patterns obtained using high pressure x-ray units was it possible to index the retained phase adequately. Since Katzman, et al. do not report the positions or intensities of the lines they observed, it is not possible to determine the extent to which the factors of preferred orientation and strain explain the differences between the two proposed structures for the high pressure phase of Cd_3As_2.

The x-ray results at atmospheric pressure on the retained Zn_3As_2 samples suggest two possibilities: (1) that the high pressure phase cannot be retained from ~60 kbars at ~115°K, or (2) that 600°C at 60 to 65 kbars is a point near the phase boundary between the tetragonal and trigonal or cubic phases, which results in the presence of more than one phase during annealing, due to pressure and temperature gradients in the sample cavity. Since the retained Zn_3As_2 samples were always badly fragmented (which has not been found for retained phases of Cd_3As_2 and InSb), the first explanation is more probable.

M. D. Banus
Mary C. Lavine

J. MAGNETIC AND OPTICAL PROPERTIES OF THE HIGH AND LOW PRESSURE FORMS OF $CsCoF_3$

The high and low pressure forms of $CsCoF_3$ contain cubic and hexagonal close packed CsF_3 layers with Co^{2+} ions occupying the fluorine octahedra between these layers. In the atmospheric pressure form (APF) (Ref. 67), one-third of the layers are cubic close packed (c) and two-thirds are hexagonal close packed (h), giving a nine-layer (9L) structure with the stacking sequence hhchhchhc and hexagonal cell dimensions 6.20 Å × 22.36 Å [Fig. II-22(a)]. The high pressure form[68] is obtained by quenching the compound from 700°C at pressures greater than 20 kbars. In this structure two-thirds of the layers are cubic close packed, giving the six-layer (6L) stacking sequence cchccch of Fig. II-22(b) with hexagonal cell dimensions 6.09 Å × 14.67 Å. This 6L structure is also found for the ferrimagnetic forms of $RbNiF_3$ (Ref. 69) and $CsNiF_3$ (Ref. 70).

Magnetic susceptibility measurements on both forms of $CsCoF_3$ have been made, using a vibrating sample magnetometer, from room temperature to 4.2°K and in fields up to 17 kOe. The atmospheric pressure form (9L) is characterized at low temperature by a Néel point T_N = 8°K. At 4.2°K the magnetization and its field dependence, Fig. II-23, show a large increase between 8 and 10 kOe, which is consistent with a reorientation of the Co^{2+} spins. At 77°K and at room temperature the field dependence of the magnetization is linear.

Deviation from a Curie-Weiss law below 70°K, Fig. II-24, is consistent with ferromagnetic ordering within the Co^{2+}-ion triples showing common octahedral-site faces. However, long range antiferromagnetic order occurs only below 8°K because the antiferromagnetic 180° Co^{2+}-F-Co^{2+} interactions are relatively weak. Such antiferromagnetic order would double the unit cell along the c axis.

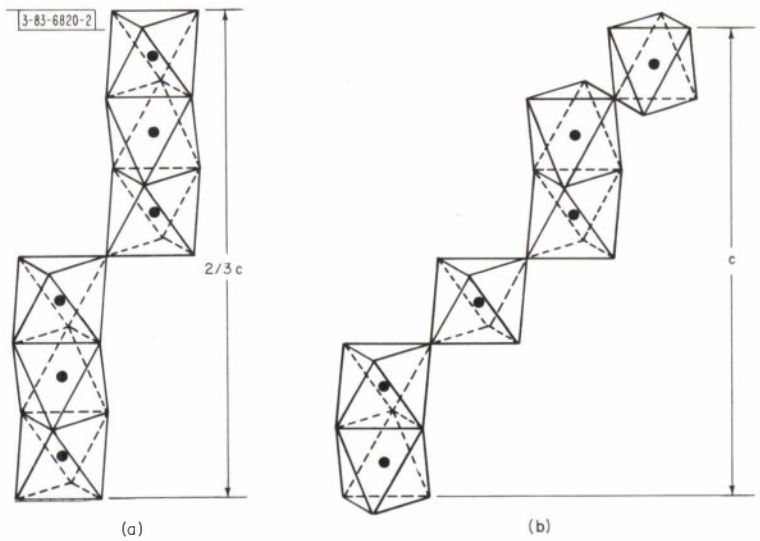

Fig. II-22. Octahedra linkage far (a) hexaganal (9L) structure and (b) hexaganal (6L) structure af $CsCaF_3$.

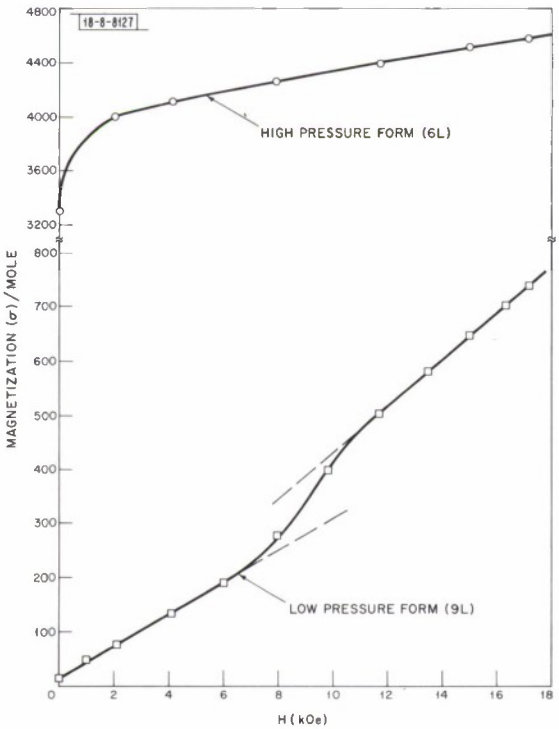

Fig. II-23. Magnetizatian vs magnetic field at 4.2°K far atmaspheric pressure (9L) and high pressure (6L) farms af $CsCaF_3$.

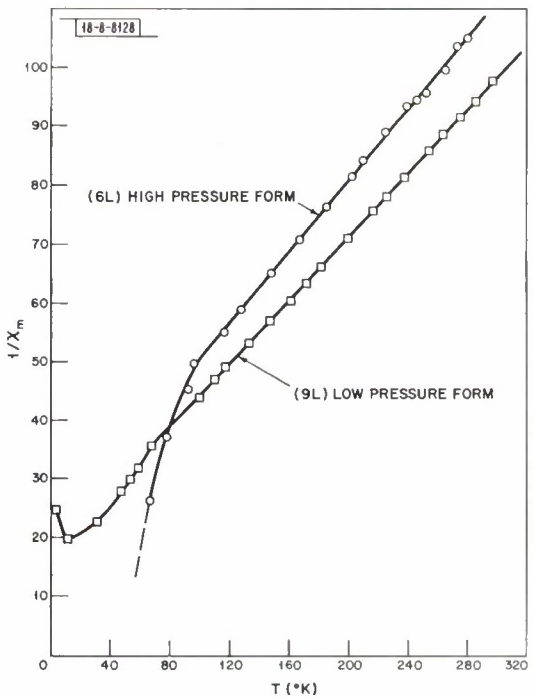

Fig. II-24. Inverse malar susceptibility ($1/\chi_m$) vs temperature far atmaspheric pressure (9L) and high pressure (6L) farms af $CsCaF_3$.

Above 70°K, the susceptibility obeys the Curie-Weiss law with $C_m = 3.70$ ($\mu_{eff}^{Co^{2+}} = 5.4\mu_B$) and $\Theta_p = -62$°K (Fig. II-24). This is in good agreement with the original work of Rudorff, et al.,[69] who examined the susceptibility over the temperature range 77° to 475°K and found a $C_m = 3.65$ and a $\Theta_p = -60$°K. The value of $\mu_{eff}^{Co^{2+}}$ is as expected for high spin Co^{2+} in a slightly distorted octahedral site.

The magnetic properties of the high pressure form (6L) of $CsCoF_3$ are quite different from those of the atmospheric pressure form. This phase exhibits a ferrimagnetic transition at $T_C = 50$°K. The saturation magnetization at 17.2 kOe and 4.2°K is $0.8\mu_B$/Co. The magnetic susceptibility obeys the Curie-Weiss law for $T > 100$°K with $C_m = 3.3$ ($\mu_{eff}^{Co^{2+}} = 5.1\mu_B$) and $\Theta_p = -65$°K (Fig. II-24). The magnetic ordering is probably the same as for the 6L forms of $RbNiF_3$, $CsNiF_3$ and $CsFeF_3$, in which the face-shared pairs are ferromagnetically ordered with antiferromagnetic 180° Co^{2+}-F-Co^{2+} interactions between corner-shared octahedra. In the 6L structure of $CsCoF_3$ this would align four Co spins in one direction and two in the opposite direction. Since each octahedral-site Co^{2+} ion has a net atomic moment of about $3.7\mu_B$, as can be determined from the magnetization of $CoFe_2O_4$ and $CoMnO_3$, this ordering predicts an average of $1.23\mu_B$ per Co^{2+} ion. The saturation magnetization found for this phase of $CsCoF_3$ ($0.8\mu_B$/Co) is well below this value. The decrease can be attributed to a large anisotropy in this hexagonal structure, the magnetization still remaining unsaturated at 17.2 kOe, as can be seen from Fig. II-23.

Optical transmission measurements with double beam spectrometers in the range of 0.2 to 16 μm were made on 6L and 9L $CsCoF_3$ powders hot pressed into KBr disks or suspended in index-matching liquids. Diffuse reflection measurements on $CsCoF_3$ powders were made at visible and near infrared wavelengths.

Thus far we have made the following observations:

(1) Both 6L and 9L have approximately the same optical spectra, but the intensities of several absorptions vary markedly. The data show that the Co^{+2} ion in $CsCoF_3$ is in a sufficiently distorted octahedral site that strong trigonal crystal fields are present.

(2) Multi-phonon spectra are observed for both crystal modifications. Phonon assignments are not yet complete.

(3) The Co^{+2} ions in the high pressure (6L) form are acted on by stronger trigonal crystal fields. Energy levels for the 6L form are higher and cause it to look somewhat blue in reflection. The 9L form has the pink color commonly associated with Co^{+2} ions in octahedral sites.

(4) For both phases, $Dq \approx 760\,cm^{-1}$, spin-orbit interaction parameter $\zeta \approx 500\,cm^{-1}$, and long-wavelength cutoff ≈ 13 μm.

J. M. Longo
J. A. Kafalas
J. R. O'Connor
T. W. Hilton
D. A. Batson

K. CHEMICAL ANALYSIS BY AUTOMATIC PHOTOMETRIC EDTA TITRATIONS

Many analytical methods for the determination of metallic elements are based on titrations with EDTA solutions. Frequently a potentiometric end point can be employed. In this case the titration can be performed automatically by using a recording potentiometer-titrator to measure the EMF of the solution-sensor electrode half cell, control a mechanical burette which introduces

the reagent, and sense the end point. A relative precision of one to three parts per thousand can be achieved by this method.

For many titrations, however, a potentiometric end point cannot be used because of difficulty in controlling the electrolyte solution or because the solution poisons the sensing electrodes. The end points of these titrations are usually estimated visually, by observing the color change of an appropriate indicator which has been added to the solution. Because of the uncertainty of visual observation, however, relative precision as high as three parts per thousand is rarely achieved by this method. In an attempt to obtain precision of this order for a larger number of titrations with color change end points, we have developed a method for automatic photometric titrations which employs a spectrophotometer as a transducer to convert color (or more precisely, optical density at a fixed wavelength) to EMF for measurement by the potentiometer-titrator.

The cell compartment of a Cary Model 11 spectrophotometer was modified to hold a 250-ml beaker containing the sample solution in a fixed position in the light path and to provide means for stirring the solution and delivering the titrant without opening the compartment. A 10-turn variable resistor was coupled mechanically with the pen drive motor of the spectrophotometer recorder so that its resistance increases linearly with the motion of the pen from zero to full scale. A 6-V battery and additional resistors were connected in series to provide a suitable voltage drop across the variable resistor for measurement by the potentiometer-titrator, which controls a mechanical burette in the same manner as in potentiometric titration.

Initial tests have been made to see whether the same precision can be achieved with the new photometric system as with our automatic potentiometric system, using the same titrants. The titrations were carried out with known quantities of zinc and a 0.01 M EDTA solution. In the potentiometric titration, mercury cup and standard calomel electrodes were used. Eriochrome black T was the indicator used in the photometric titration. The tests showed that a relative precision of about two parts per thousand can be achieved by both systems.

E. B. Owens
Isabel H. Searles

REFERENCES

1. C. F. Guerci and M. W. Shafer, J. Appl. Phys. 37, 1406 (1966).
2. T. B. Reed, Mat. Res. Bull. 2, 349 (1967).
3. T. B. Reed and R. E. Fahey, Rev. Sci. Instr. 37, 59 (1966).
4. J. F. Miller, J. Electrochem. Soc. 106, 1043 (1959).
5. F. Holtzberg, private communication.
6. E. R. Pollard, "Electronic Properties of Niobium Monoxide", Ph.D. Thesis, Department of Material Sciences, M. I. T. (1968).
7. Solid State Research Report, Lincoln Laboratory, M. I. T. (1969:2), p. 17, DDC AD-690997.
8. T. B. Reed and E. R. Pollard, J. Cryst. Growth 2, 243 (1968).
9. A. D. Stuckes and G. Farrell, J. Phys. Chem. Solids 25, 477 (1964).
10. J. Litwin, Phys. Stat. Sol. 5, 551 (1964).
11. L. V. Prytkina, V. V. Volkov, A. N. Mentser, A. V. Vanyukov, and P. S. Kireev, Sov. Phys. Semicon. 2, 509 (1968).
12. J. M. Steininger and A. J. Strauss, Extended Abs., Electrochem. Soc. Meeting (New York, Spring, 1969), p. 274.
13. Solid State Research Report, Lincoln Laboratory, M. I. T. (1969:1), p. 33, DDC AD-687100.
14. B. M. Kulwicki, "The Phase Equilibria of Some Compound Semiconductors by DTA Calorimetry," Ph. D. Thesis, University of Michigan (1963).
15. H. Tubota, Japan. J. Appl. Phys. 2, 259 (1963).
16. R. A. Burmeister and D. A. Stevenson, Phys. Stat. Sol. 24, 683 (1967).
17. J. M. Steininger, Mat. Res. Bull. 3, 595 (1968).
18. M. Aven and H. H. Woodbury, Appl. Phys. Letters 1, 53 (1962).
19. Solid State Research Report, Lincoln Laboratory, M. I. T. (1969:2), p. 11, DDC AD-690997.
20. F. A. Kröger, Chemistry of Imperfect Crystals (North-Holland Publishing Co., Amsterdam, 1964), p. 249.
21. P. M. Borsenberger, D. A. Stevenson, and R. A. Burmeister, Proc. 1967 Int. Conf. on II-VI Semiconducting Compounds, D. Thomas, ed., (W. A. Benjamin, Inc., New York, 1967), p. 439.
22. A. Magneli, Arkiv Kemi Min. Geol. 15B, No. 3 (1941).
23. J. B. Taylor and R. D. Heyding, Can. J. Chem. 36, 597 (1958).
24. G. Blasse, J. Inorg. Nucl. Chem. 28, 1122 (1966).
25. H. M. Kasper, Mat. Res. Bull. 4, 33 (1969).
26. J. M. Longo, private communication.
27. H. M. Kasper, Inorg. Chem. 8, 1000 (1969).
28. _____, Z. anorg. allgem. Chem. 356, 329 (1968).
29. _____, Z. phys. Chem. N. F. (Frankfurt) 58, 148 (1968).
30. F. A. Kröger, Some Aspects of the Luminescence of Solids (Elsevier Publishing Co., Amsterdam, 1948), Chap. 11.
31. F. Gaume-Mahn, Compt. Rend. Acad. Sci. Paris 265B, 1047 (1967).
32. K. Brandt, Arkiv Kemi Min. Geol. 17A, No. 15, 1 (1943).
33. H. M. Kasper, Monatsh. Chem. 98, 2104 (1967).
34. A. Zalkin, J. D. Forrester, and D. H. Templeton, Acta Cryst. 17, 1408 (1964).
35. S. Natansohn, J. Inorg. Nucl. Chem. 30, 741 (1968).
36. E. Stanley, Acta Cryst. 9, 897 (1956).

37. A. D. Wadsley, Acta Cryst. 8, 695 (1955); 10, 261 (1957).
38. J. Darriet, Thesis, U. of Bordeaux (1967).
39. J. Galy and J. Darriet, private communication.
40. M. Pouchard, Thesis, U. of Bordeaux (1967).
41. A. Casalot, Thesis, U. of Bordeaux (1968).
42. R. P. Ozerov, Sov. Phys. Cryst. 2, 219 (1957); 4, 181 (1959); Russ. J. Inorg. Chem. 4, 476 (1959).
43. J. B. Sohn, Ph. D. Thesis, Cornell U. (1965); M. J. Sienko and J. B. Sohn, J. Chem. Phys. 44, 1369 (1966).
44. A. Casalot and P. Hagenmuller, J. Phys. Chem. Solids 30, 1341 (1969).
45. J. B. Goodenough, "Metallic Oxides," in Progress in Solid State Chemistry, H. Reiss, ed. (Pergamon Press, New York), Vol. 5, to be published.
46. A. Casalot, J. Darriet, and J. Galy, private communication.
47. O. Inkinen and P. Suortti, Ann. Acad. Sci. Fenn. A II 147 (1964).
48. M. Diana, G. Mazzone, and J. J. DeMarco, Phys. Rev., to be published.
49. D. T. Cromer, Acta Cryst. 18, 17 (1965).
50. M. J. Cooper, Acta Cryst. 18, 813 (1965).
51. G. D. Hughes, J. B. Woodhouse, and I. A. Bucklow, Brit. J. Appl. Phys. 1, 695 (1968).
52. R. D. Deslattes, A. F. O. S. R. Report No. TN-58-784 (1958).
53. R. W. Carter, R. H. Rohrer, W. H. Carlton, and G. R. Dyer, Health Physics 13, 593 (1967).
54. P. A. Doyle and P. S. Turner, Acta Cryst. A24, 390 (1968).
55. P. M. Raccah and V. E. Henrich, Phys. Rev., to be published.
56. H. W. T. Barron and T. Smith, J. Phys. Chem. Solids 27, 1951 (1966).
57. A. Jayaraman, T. R. Anantharaman, and W. Klement, Jr., J. Phys. Chem. Solids 27, 1605 (1966).
58. H. Katzman, T. Donohue, and W. F. Libby, Phys. Rev. Letters 20, 442 (1968).
59. Solid State Research Report, Lincoln Laboratory, M. I. T. (1968:1), 19, DDC AD-668762.
60. Solid State Research Report, Lincoln Laboratory, M. I. T. (1968:1), 20, DDC AD-668762.
61. G. A. Steigman and J. Goodyear, Acta Cryst. B24, 1062 (1968).
62. H. Cole, F. W. Chambers, and H. M. Dunn, Acta Cryst. 9, 685 (1956).
63. G. J. Piermarini and C. R. Wier, J. Res. Nat. Bur. Stds. 66a, 325 (1962).
64. W. A. Bassett, T. Takahashi, and P. W. Stook, Rev. Sci. Instr. 38, 37 (1967).
65. M. D. Banus and M. C. Lavine, J. Appl. Phys. 38, 2042 (1967).
66. _____, J. Appl. Phys. 40, 409 (1969).
67. D. Babel, Structure and Bonding 3, 1 (1967).
68. J. M. Longo and J. A. Kafalas, J. Solid State Chem. 1, 103 (1969).
69. W. Rudorff, J. Kändler, and D. Babel, Z. anorg. allgem. Chem. 317, 261 (1962).
70. J. M. Longo and J. A. Kafalas, J. Appl. Phys. 40, 1601 (1969).

III. PHYSICS OF SOLIDS

A. ELECTRONIC BAND STRUCTURE

1. Infrared Cyclotron Resonance and Related Experiments in the Conduction Band of InSb

A comprehensive study of the conduction band of InSb has been carried out. Fundamental cyclotron resonance transitions involving the lowest Landau levels and both spin states are observed over a range of magnetic fields from 5 to 35 kG. Additional transitions involving impurities, phonons, cyclotron resonance harmonics, and spin-flip are also studied. The fundamental cyclotron resonance and the spin-flip cyclotron resonance, together with the spin resonance results of Isaacson,[1] are analyzed in terms of a nonparabolic band theory involving interactions with the six valence bands and allowing the possibility of interactions with more remote bands. A good fit to the nonparabolic band theory is obtained when one is careful to remove effects due to impurities and the electron-phonon interaction. A band edge effective mass of 0.0139 m and a band edge g-factor of −51.3 are obtained. An analysis using these values shows that remote band interactions contribute to the value of either the mass or g-factor or both by an amount on the order of 10 percent.

The transition energies for cyclotron resonance harmonics, spin-flip transitions, phonon assisted cyclotron resonance, and spin resonance as a function of Fermi level, have been calculated and give a good fit to the data. This confirms the identification of these transitions and shows that the nonparabolic theory gives the magnetic energy levels correctly to energies as high as 60 meV. A value of 24.4 meV is found for the LO phonon energy. The existence of the phonon-assisted cyclotron resonance is explained on the basis of the mixing of Landau levels by the electron-phonon interaction. The strength of the cyclotron resonance harmonics is not satisfactorily explained, although several possible mechanisms are proposed. An H = 0 electron energy dispersion relation and other related band properties are deduced from the magnetic field results, and compared to other experiments. This research is being submitted for publication.

E. J. Johnson
D. H. Dickey (Optics Division)

2. Polaron Cyclotron Resonance in CdTe

The effective mass of polarons in CdTe was measured at 4.2°K by observing cyclotron resonance using a carcinotron radiating at 901μ and the HCN and DCN laser lines at 337μ and 195μ, respectively. The experimental values are given in Table III-1 along with the results of a variational calculation for the $\ell = 0$ and $\ell = 1$ polaron Landau levels[2] based on an extension to finite magnetic fields of the zero field polaron energy spectrum calculation of Larsen.[3] The calculation includes a small correction for the nonparabolicity of the CdTe conduction band, and gives good quantitative agreement.

The measurements were made with a 100-kG superconducting magnet. The magnetic field was measured by observing NMR in $^{27}A\ell$ simultaneously with cyclotron resonance. An NMR marginal oscillator capable of operating at frequencies up to 150 MHz was constructed for this

TABLE III-1

VARIATION WITH WAVELENGTH OF THE POLARON EFFECTIVE MASS IN CdTe†

Wavelength, λ	m^* experimental	$(m^*_\lambda / m^*_{377\mu})$ experimental	$(m^*_\lambda / m^*_{337\mu})$ thearetical‡
901μ	0.0955 ± 0.0020	0.975 ± 0.020	0.989
337μ	0.0979 ± 0.0002	1.000	1.000
195μ	0.0995 ± 0.0002	1.016 ± 0.004	1.015

† Determined from the $\ell = 0$ to $\ell = 1$ Landau level transition.

‡ Reference 2.

purpose. The NMR probe allowed high precision measurements of the eyelotron resonance peak, accurate to 0.2 percent, to be made at 337 and 195μ. The mueh greater uncertainty of the 901μ measurement is due to the 2 percent uncertainty in wavelength.

In addition, an effective mass $m^* = (0.1024 \pm 0.0005)\,m$ was measured at 118μ (H_2O laser line) at the Francis Bitter National Magnet Laboratory in collaboration with C. C. Bradley. The result, when normalized to the 337μ experimental mass, gives 1.046 ± 0.0006, in agreement with the prediction.

J. Waldman
C. D. Parker
P. E. Tannenwald

3. Positron Annihilation in Copper – Apparent Disagreements

Positron annihilation studies of the momentum distribution of electrons in single erystals of copper using "point" slits,[4] rectangular slits,[5,6] and wide slits[7] have been reported. With the first two slit geometries, annihilations of positrons with conduction eleetrons whose momenta are in the necks of the copper Fermi surface are elearly detected.

We have estimated the expected increase in counting ratc due to the necks by using thc single, non-interaeting, particle approach. This estimate is a factor of two smaller than the rectangular slit result[5,6] and somewhat larger than the point slit result.[4] From thc wide slit measurements[7] we have derived the cxpectcd nonconduetion electron contribution to the rectangular slit angular correlation curve; it agrees with the measured result[6] within 8 percent, falling off somewhat more slowly with increasing angle.

J. Melngailis

B. MAGNETISM

1. Magnetic Ordering Effects on the Reflectivity of EuS and EuSe†

Our earlier observations of the effect of ferromagnetie ordering on the reflectivity of EuO (Ref. 8) have provided direet cvidcnee for the spin polarization of the conduction band in this

† Part of this work was carried out at the Francis Bitter National Magnet Laboratory, M.I.T.

ferromagnetic semiconductor, and suggest that the optical absorption edge is due to a transition from the localized $4f^7$ ground state of the Eu^{2+} ion to a final state configuration comprised of an excited $4f^6$ multiplet and an electron in an apparently narrow $5d(t_{2g})$ band.

Since the transition in this model involves primarily the electrons of thc Eu^{2+} ion, we would predict that effects similar to those observed in EuO should exist in the other Eu chalcogenide semiconductors, EuS and EuSe. We have now made measurements of the temperature dependent reflectivity, and the reflectivity of circularly polarized light in an orienting magnetic field of the E_1 reflectivity peak associated with the absorption edges of EuS (~1.6 eV) and EuSe (1.8 eV). We observe similar behavior among all Eu ferromagnetic semiconductors in support of the proposed model.

As described for EuO, for both EuS and EuSe the E_1 reflectivity peak moves to lower energy as the temperature is reduced through the respective magnetic ordering temperatures of 16.5° and 4.8°K. EuS is ferromagnetic at the ordering temperature, but EuSe is metamagnetic and becomes ferromagnetic when an external field is applied below the ordering temperature. In addition to the red-shift the line shape changes, suggesting that the E_1 peak is split into three peaks.

This splitting is clearly seen using polarized light and an orienting magnetic field as shown in Figs. III-1 and III-2. At 1.5°K the E_1 peak in both EuS and EuSe exhibits a triplet structure in which the lowest energy peak E_1' has a pure σ_R polarization, the E_1'' peak is nearly pure σ_L, and the central E_1 peak has both polarizations although σ_R is stronger. The results for EuO, EuS and EuSe in the ferromagnetic state are therefore very similar except that the location in energy of position of the E_1 peak is different. For all three materials the splitting of the side peaks from the central one are about 0.25 eV.

The polarization dependence was also measured at 22°K which is just above T_c for EuS but more than four times greater than T_c for EuSe. However, in both cases, a doublet structure is clearly resolved as seen in the figures.

As previously described for EuO, the doublet structure can be understood in terms of the transition probabilities for left and right circularly polarized light for the transition $4f^7(^8S_{7/2}) \rightarrow 4f^6(^7F_J)\ 5d(t_{2g})$. It is resolved for this transition when the ground state $M_s = -7/2$ level is preferentially populated at low temperatures in a magnetic ficld. However even well above T_c, there is a large induced magnetization when a large external field is applied, thus the doublet is still observed in EuSe at 22°K. The triplet in the ferromagnetic state arises from the exchange splitting of the final state of the transition which is the 5d conduction band, and this exchange splitting appears to be the same for all these materials.

This work has been accepted for publication in Solid State Communications.

J. Feinleib
W. J. Scouler
C. R. Pidgeon†
J. O. Dimmock
J. Hanus
T. B. Reed

2. New Electron Spin Waves in Nonmagnetic Conductors

In recent years, considerable interest has centered on the prediction and observation of the effect on electron plasma collective modes of electron-electron correlations other than those

† Francis Bitter National Magnet Laboratory, M.I.T.

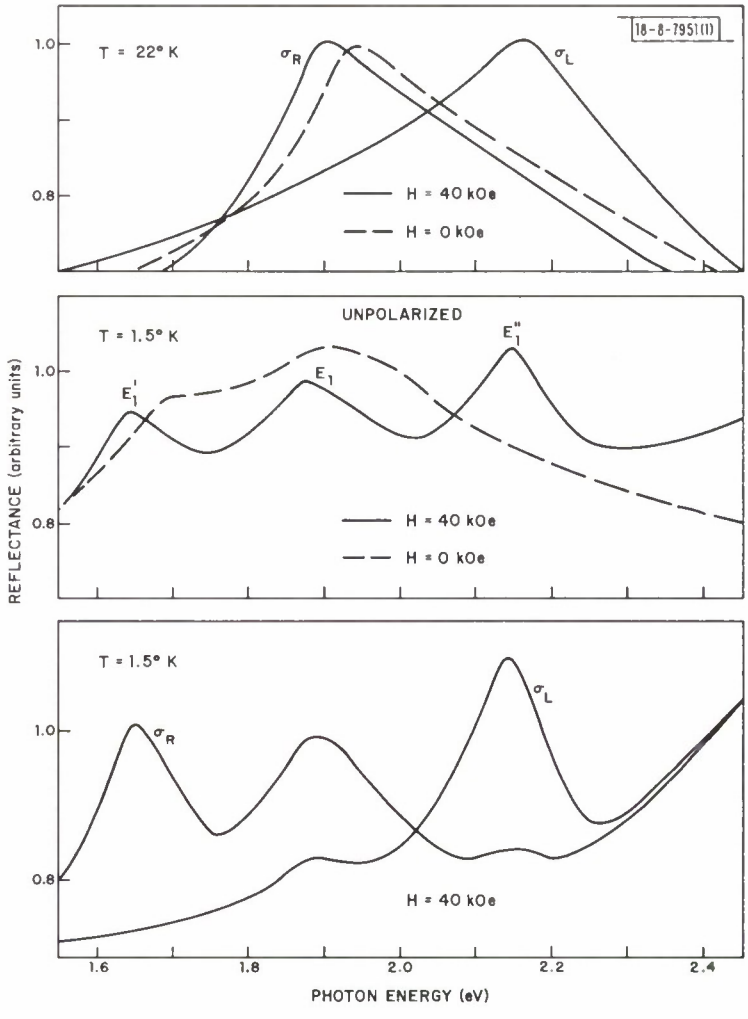

Fig. III-1. Palarized and unpalarized reflectivity af EuS in a magnetic field at 1.5°K and 22°K.

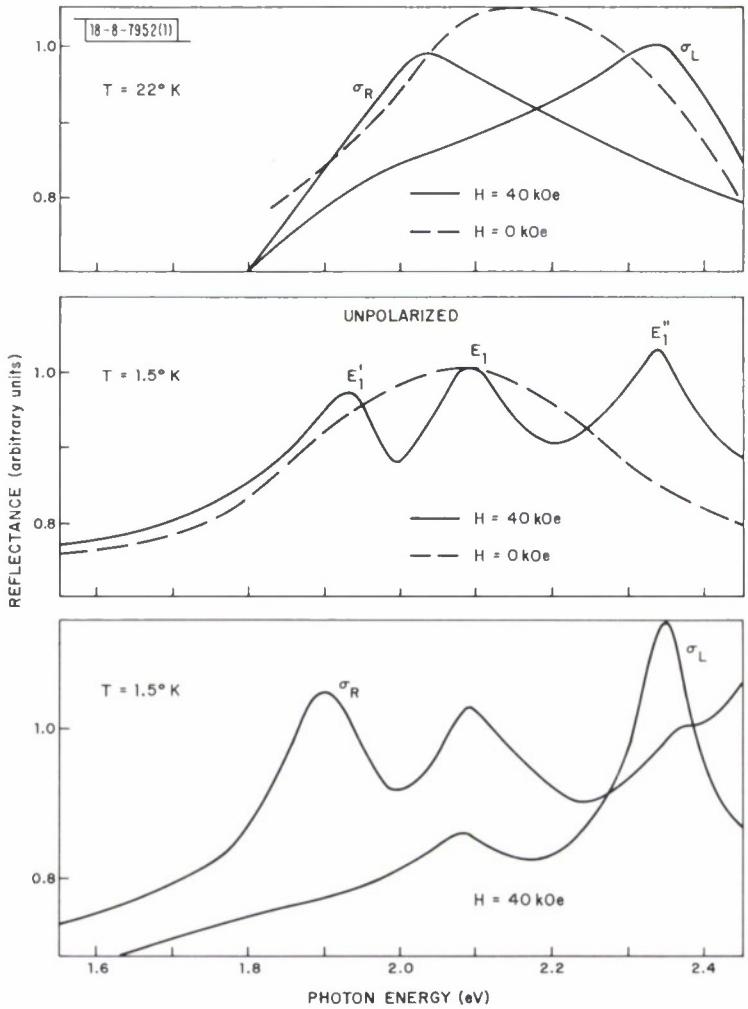

Fig. III-2. Polorized and unpolarized reflectivity of EuSe in a magnetic field ot 1.5°K and 22°K.

embodied in the Coulomb self-consistent field.[9-16] The phenomenological short range interactions of the Landau Fermi liquid theory[17] have generally been used as a basis for prediction of: (1) the modification of the dispersion relations of known plasma modes,[14-16] and (2) the presence of new collective modes[9-14] which owe their existence entirely to these "other" (Fermi liquid) interactions.

Most interesting are phenomena in the latter category, perhaps the most dramatic example being the observation by Schultz and Dunifer[9] of conduction electron spin waves in the alkali metals. Since spin waves would not otherwise be expected to exist in nonferromagnetic metals, the existence of these waves has been taken as direct verification[10] of the importance of short range exchange interactions[11] as postulated in Fermi liquid theory.

It has been pointed out in a preliminary publication[18] that, even when explicit exchange interactions are unimportant, electron spin waves can occur in nonmagnetic conductors due to spin-orbit coupling and the long range Coulomb field of the electrons. This totally different mechanism leads to spin wave properties which depend intimately upon the fact that the electrons are in a solid and which are not generally coincident with the properties resulting from Fermi-liquid correlations. Although a study of this new spin wave mechanism is of interest in itself, the effect has a second significance: when interpreting experimental results in general, it is important to consider the possible contribution of both mechanisms to the properties of observed waves. In the absence of exchange interactions, these spin-orbit-induced spin waves constitute a new mode of wave propagation for carriers in nonmagnetic solids.

Spin-orbit coupling[19] mixes the orbital (space) and spin character of the electron wave functions so that they are no longer eigenstates of the spin operator σ_z. However, for crystals with inversion symmetry the eigenstates occur naturally in degenerate pairs (in zero magnetic field). The degeneracy of these spin conjugate pairs is split by a static magnetic field. Resonant excitation of electrons between these states in a magnetic field is a generalization of simple electron spin resonance (ESR).† Without spin-orbit coupling, excitation of electrons between opposite spin states requires application of a perturbation which couples directly to the spin, e.g., an oscillating magnetic field. With spin-orbit coupling, a perturbation which adds only a "space like" term to the Hamiltonian, e.g., an oscillating electric field, can induce spin flip transitions. In the same manner, the long range Coulomb forces between electrons act through spin-orbit coupling to correlate the motion of electrons with opposite sign, leading to the described spin waves.

Under rather general circumstances in the long wavelength limit, it can be shown[18] that for propagation perpendicular to a dc magnetic field ($\vec{q} \perp \vec{B}_o$) (defining the single electron spin flip frequency as ω_s), the dispersion relation for the spin wave is given by

$$\omega^2 - \omega_s^2 = \omega_s \Delta\omega \left[\frac{\omega_c^2 - \omega_s^2}{\omega_p^2 + \omega_c^2 - \omega_s^2} \right] + O(q_\perp^2) \quad , \tag{III-1}$$

where ω_p is the conduction band plasma frequency and ω_c is the electron cyclotron frequency. As a first approximation, any dependence of ω_s on the orbital quantum numbers has been neglected

† Common terminology such as ESR, spin flip, opposite spin, etc. will be used in what follows even though such terms are not strictly appropriate when spin-orbit coupling is important. Generally no confusion results, particularly for weak coupling.

in this example. The quantity $\Delta\omega$ goes as the spin density of the electron gas, vanishes for zero spin-orbit interaction, and is independent of $q_\perp$; its specific form depends on the details of the wave functions for the material considered. Note that the leading term on the right of Eq. (III-1) is independent of $q_\perp$,† as contrasted with the Fermi liquid spin waves[10-12] which have a corresponding term of $O(q_\perp^2)$. The spin waves considered here are further distinguished from the Fermi liquid type by the fact that they are not generally expected to be observable for $\vec{q} \parallel \vec{B}_o$. Also, for the alkali metals, since the spin-orbit interaction is very small, the estimated spin wave frequencies are shifted from the ESR line by amounts much smaller than those observed.[9]

As an example of a tractable calculation, $\Delta\omega$ can be calculated for doped (n-type) semiconductors, such as indium antimonide. In high magnetic fields where only the lowest Landau level (with orbital quantum number $\ell = 0$, spin up) is occupied, we find,‡§ for $\vec{q} \perp \vec{B}_o$, and densities and magnetic fields considered below (T = 0),

$$\frac{\omega - \omega_{so}}{\omega_{so}} \approx \frac{\pi^2}{8} \left(\frac{m^*}{m}\right)^2 (g^* - g)^2 \left(\frac{\Delta + 2E_g}{\Delta + E_g}\right)^2 \frac{E_F}{E_g} \frac{\hbar\omega_p^2}{E_g \omega_{so}} \times \left[\frac{\omega_c^2 - \omega_{so}^2}{\omega_p^2 + \omega_c^2 - \omega_{so}^2}\right]^2 + O(q_\perp^2 r_c^2) \qquad \text{(III-2)}$$

where ω_{so} is the band edge ($k_z = 0$) spin flip frequency, m^* is the conduction band effective mass, Δ is the valence band spin-orbit energy, E_F is the Fermi energy, and r_c is the cyclotron radius of an electron in the $\ell = 0$ level. Note, as the spin-orbit parameter (Δ/E_g) approaches 0, the effective g-factor g^* approaches the free electron g and the frequency shift goes to zero. For InSb with donor concentrations of about $10^{17}\,cm^{-3}$ and magnetic fields around 100 kG, Eq. (III-2) yields $(\omega - \omega_{so})/\omega_{so} \approx 0.01$ and $\omega_{so} \approx 190\,cm^{-1}$. Although this frequency shift is small, effects due to these spin waves might be observed in high resolution infrared inelastic light scattering or slab transmission experiments. Rather narrow spin flip line widths ($\lesssim$ a few cm^{-1}) have been observed[20] in scattering experiments in InSb and InAs with $\vec{q}$ oblique to $\vec{B}_o$. Further study for InSb shows that the term of order $q_\perp^2 r_c^2$ in Eq. (III-2) is negative, leading to the lowest dispersion curve shown qualitatively in Fig. III-3.

One also expects spin waves near combined transition (orbital plus a spin change) energies $\hbar(N\omega_c \pm \omega_s)$, where $N \equiv |\Delta\ell| \geq 1$.¶ For n-InSb with $\vec{q} \perp \vec{B}_o$, it can be shown that for these "combined" spin waves $\omega = (N\omega_c \pm \omega_s) + O(q_\perp^2 r_c^2)^N$, leading to a frequency shift (from combined ESR) which vanishes in the long wavelength limit. The dispersion for these waves is shown qualitatively

† This q-independent frequency shift should not be taken to correspond to a many-electron shift in the one electron g-factor. For the specific problem being considered, the appropriate response function will have poles both at ω_s and the solutions of Eq. (III-1).

‡ In this calculation we use the two-band model for InSb. Also, a consistent calculation required inclusion of the k_z dependence of ω_s.

§ All discussion in this paper refers to crystals which have inversion symmetry. In general, one expects inversion asymmetry to enhance the magnitude of the spin flip matrix element and introduce anisotropy effects which depend on the direction of B_o in the crystal. The InSb zinc-blende crystal structure lacks inversion symmetry. However, for conditions considered here this effect is small.[19]

¶ We are loosely neglecting nonparabolicity effects here in order not to cloud the qualitative features. For a discussion of combined transitions in InSb, see Ref. 21.

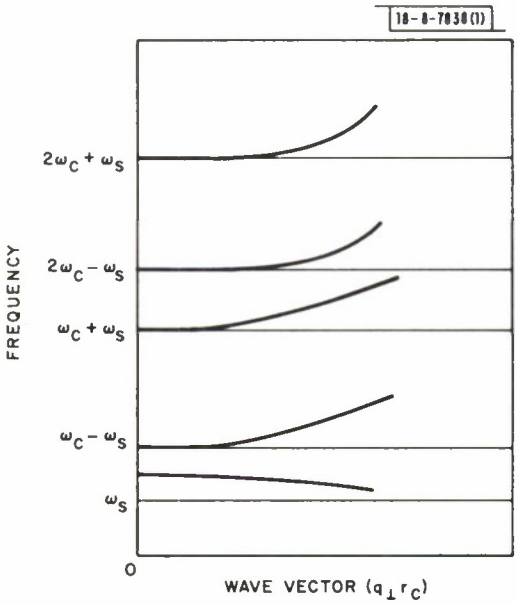

Fig. III-3. Quolitotive long wovelength dispersion curves for spin-orbit-induced electron spin woves propagating perpendiculor to mognetic field in n-InSb. For disploy purposes, frequency shifts ore exoggerated ond scoles ore arbitrory.

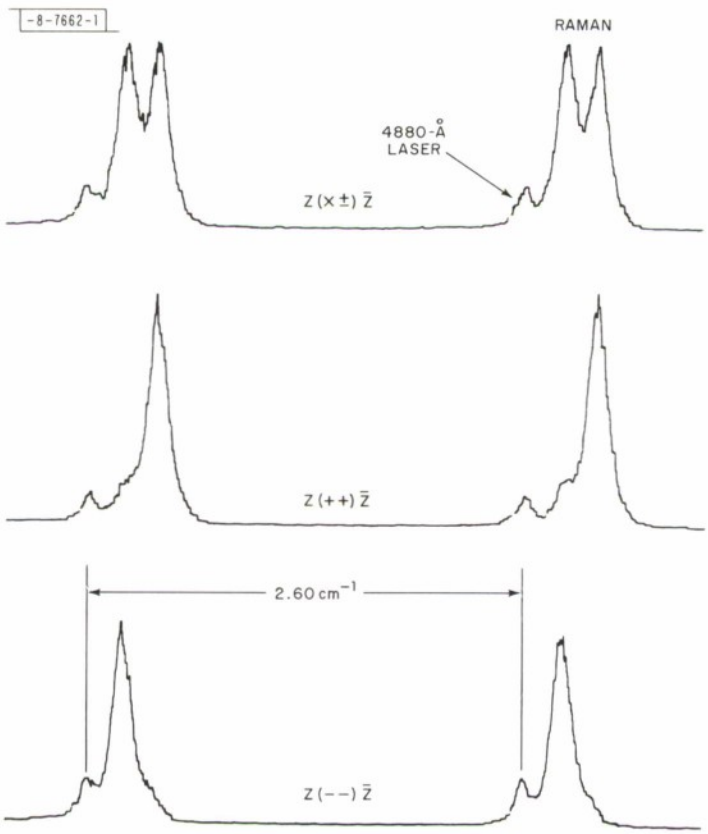

Fig. III-4. 5°K, 128-cm^{-1} Romon line in o-quortz illustroting polorizotion properties of lineor wovevector doublet.

by the upper curves in Fig. III-3. The combined spin waves would be difficult to observe due to their small frequency shifts and residues.

F. A. Blum, Jr.

C. LASER SCATTERING

1. Linear Wavevector Shifts in the Raman Spectrum of α-Quartz and Infrared Optical Activity

Fine structure has been observed in the low temperature Raman spectrum of the 128 cm^{-1} E-mode in α-quartz. This structure is a manifestation of an allowed linear dependence of the optical phonon frequency with wavevector. Since Raman scattering probes a small but finite wavevector, it is possible to observe these frequency shifts using high resolution thermal or stimulated Raman spectroscopy. The linear splitting of the 128 cm^{-1} E-mode doublet is $(0.86 \pm 0.05) \times 10^5$ cm/sec as determined by backscattering at several laser wavelengths. The doublet is shown in Fig. III-4 in scattering from linearly polarized single mode Ar^+ laser light; the lower traces demonstrate the circular polarization selection rules.

Linear wavevector shifts may give rise to measurable optical activity in the far infrared. The theory of the strength and dispersion of infrared rotary power is developed in a more complete article to establish the connection between the two phenomena. From independently measured parameters, a peak rotary power of ~1.8 rad/cm is predicted for this E-mode resonance at 76μ in α-quartz.

A. S. Pine
G. F. Dresselhaus

2. Inelastic Light Scattering from Semiconductor Plasmas in a Magnetic Field

The cross section for the inelastic scattering of light from mobile carriers in semiconductors immersed in a dc magnetic field $\vec{B}_o$ has been calculated approximately in a manner sufficiently general to include directly particle-particle Coulomb interactions (in the random phase approximation), band structure of an arbitrary nature, and the very important virtual interband processes.[22] The effect of Coulomb interactions on the momentum matrix elements occurring in the calculation is neglected. The results encompass scattering from the various longitudinal magnetoplasma collective modes, and single particle excitations between Landau levels and spin states. Resonant enhancement factors are automatically included, as are spin-orbit-induced effects such as scattering from spin density fluctuations and spin waves. Low temperature electrons in semiconductors, such as indium antimonide, were used as a specific example to illustrate general features of the scattering for the two major geometries: $\vec{q} \perp \vec{B}_o$ and $\vec{q} \parallel \vec{B}_o$, where $\vec{q}$ is the scattering wavevector. For $\vec{q} \perp \vec{B}_o$, inter-Landau-level scattering was shown to suffer significant screening due to Coulomb interactions. Also, in this geometry it was shown that the strength of the scattering from the Bernstein modes is of the order of the strength for the associated inter-Landau-level excitation.

A manuscript giving the results of this calculation has been submitted for publication.

F. A. Blum, Jr.

REFERENCES

1. R.A. Isaacson, Phys. Rev. 169, 312 (1968); for earlier work see G. Bemski, Phys. Rev. Letters 4, 62 (1960).
2. D.M. Larsen (private communication).
3. _____, Phys. Rev. 144, 697 (1966).
4. D.L. Williams, E.H. Becker, P. Petijevich and G. Jones, Phys. Rev. Letters 20, 448 (1968).
5. O. Sueoka, J. Phys. Soc. Japan 23, 1246 (1967).
6. K. Fujiwara and O. Sueoka, J. Phys. Soc. Japan 21, 1947 (1966).
7. S. Berko and J.S. Plaskett, Phys. Rev. 112, 1877 (1958).
8. J. Feinleib, W.J. Scouler, J.O. Dimmock, J. Hanus, T.B. Reed and C.R. Pidgeon, Phys. Rev. Letters 22, 1386 (1969).
9. S. Schultz and G. Dunifer, Phys. Rev. Letters 18, 283 (1967); G. Dunifer, S. Schultz and P.H. Schmidt, J. Appl. Phys. 39, 397 (1968).
10. P.M. Platzman and P.A. Wolff, Phys. Rev. Letters 18, 280 (1967).
11. V.P. Silin, Zhur. Eksp. i. Teoret. Fiz. 33, 1227 (1957) [translation: Soviet Phys. – JETP 6, 945 (1958)]; Zhur. Eksp. i. Teoret. Fiz. 35, 1243 (1958) [translation: Soviet Phys. – JETP 8, 870 (1959)].
12. D.M. Edwards, J. Phys. 2, (Pt. C) 84 (London 1969); A.R.M. Wilson, Ph.D. Thesis, Oxford (June 1968, unpublished).
13. Y.C. Cheng, J.S. Clarke and N.D. Mermin, Phys. Rev. Letters 20, 1486 (1968); G.A. Baraff, C.C. Grimes and P.M. Platzman, Phys. Rev. Letters 22, 590 (1969).
14. B.J. McIntyre, S.C. Ying and J.J. Quinn, Phys. Rev. Letters 21, 1244 (1968).
15. P.M. Platzman and W.M. Walsh and E-Ni Foo, Phys. Rev. 172, 689 (1968).
16. N.D. Mermin and Y.C. Cheng, Phys. Rev. Letters 20, 839 (1968); S.C. Ying and J.J. Quinn, Phys. Rev. Letters 20, 1007 (1968).
17. See, for example, D. Pines and P. Nozieres, The Theory of Quantum Liquids (W.A. Benjamin, Inc., New York, 1966).
18. F.A. Blum, Phys. Rev. Letters 23, 73 (1969).
19. For a review of conduction electron spin-orbit effects, see: Y. Yafet, Solid State Physics, Vol. 14, F. Seitz and D. Turnbull, eds. (Academic Press, New York, 1963), pp. 1-98.
20. R.E. Slusher, C.K.N. Patel and P.A. Fleury, Phys. Rev. Letters 18, 530 (1967); C.K.N. Patel and R.E. Slusher, Phys. Rev. 167, 413 (1968); C.K.N. Patel, Modern Optics, Vol. XVII (Polytechnic Press, Brooklyn, New York, 1967), p. 41.
21. B.D. McCombe, S.G. Bishop and R. Kaplan, Phys. Rev. Letters 18, 748 (1967).
22. F.A. Blum, Bull. Am. Phys. Soc. 14, 433 (1969).

DOCUMENT CONTROL DATA – R&D

(Security classification of title, body of abstract and indexing annotation must be entered when the overall report is classified)

1. ORIGINATING ACTIVITY *(Corporate author)* Lincoln Laboratory, M.I.T.	2a. REPORT SECURITY CLASSIFICATION Unclassified 2b. GROUP None

3. REPORT TITLE

Solid State Research

4. DESCRIPTIVE NOTES *(Type of report and inclusive dates)*

Quarterly Technical Summary – 1 May through 31 July 1969

5. AUTHOR(S) *(Last name, first name, initial)*

Tannenwald, Peter E.

6. REPORT DATE	7a. TOTAL NO. OF PAGES	7b. NO. OF REFS
15 August 1969	76	112

8a. CONTRACT OR GRANT NO.	9a. ORIGINATOR'S REPORT NUMBER(S)
AF 19(628)-5167 b. PROJECT NO. 649L c. d.	Solid State Research (1969:3) 9b. OTHER REPORT NO(S) *(Any other numbers that may be assigned this report)* ESD-TR-69-211

10. AVAILABILITY/LIMITATION NOTICES

This document has been approved for public release and sale; its distribution is unlimited.

11. SUPPLEMENTARY NOTES	12. SPONSORING MILITARY ACTIVITY
None	Air Force Systems Command, USAF

13. ABSTRACT

This report covers in detail the solid state research work at Lincoln Laboratory for the period 1 May through 31 July 1969. The topics covered are Solid State Device Research, Materials Research, and Physics of Solids.

14. KEY WORDS

solid state devices
materials research
magnetism
laser scattering
crystal growth
laser research
magnetic semiconductors
proton bombardment
MIS diodes
magneto-optical spectroscopy
semiconductor lasers
x-ray scattering